A&A 618, A136 (2018)
https://doi.org/10.1051/0004-6361/201732564

Astronomy & Astrophysics

"TNOs are Cool": A survey of the trans-Neptunian region

XIV. Size/albedo characterization of the Haumea family observed with *Herschel* and *Spitzer*⋆

E. Vilenius[1,2], J. Stansberry[3], T. Müller[2], M. Mueller[4,5], C. Kiss[6], P. Santos-Sanz[7], M. Mommert[8,9,12], A. Pál[6], E. Lellouch[10], J. L. Ortiz[7], N. Peixinho[11], A. Thirouin[12], P. S. Lykawka[13], J. Horner[14], R. Duffard[7], S. Fornasier[10], and A. Delsanti[15]

[1] Max-Planck-Institut für Sonnensystemforschung, Justus-von-Liebig-Weg 3, 37077 Göttingen, Germany
e-mail: vilenius@mps.mpg.de
[2] Max-Planck-Institut für extraterrestrische Physik, Postfach 1312, Giessenbachstr., 85741 Garching, Germany
[3] Space Telescope Science Institute, 3700 San Martin Drive, Baltimore, MD 21218, USA
[4] SRON Netherlands Institute for Space Research, Postbus 800, 9700 AV Groningen, The Netherlands
[5] Rijksuniversiteit Groningen, Kapteyn Astronomical Institute, Postbus 800, 9700 AV Groningen, The Netherlands
[6] Konkoly Observatory, Research Centre for Astronomy and Earth Sciences, Konkoly Thege 15-17, 1121 Budapest, Hungary
[7] Instituto de Astrofísica de Andalucía (CSIC), Glorieta de la Astronomía s/n, 18008-Granada, Spain
[8] Deutsches Zentrum für Luft- und Raumfahrt e.V., Institute of Planetary Research, Rutherfordstr. 2, 12489 Berlin, Germany
[9] Northern Arizona University, Department of Physics and Astronomy, PO Box 6010, Flagstaff, AZ 86011, USA
[10] LESIA, Observatoire de Paris, Université PSL, CNRS, Univ. Paris Diderot, Sorbonne Paris Cité, Sorbonne Université, 5 Place J. Janssen, 92195 Meudon Pricipal Cedex, France
[11] CITEUC – Centre for Earth and Space Science Research of the University of Coimbra, Observatório Astronómico da Universidade de Coimbra, 3030-004 Coimbra, Portugal
[12] Lowell Observatory, 1400 W Mars Hill Rd, Flagstaff, AZ 86001, USA
[13] School of Interdisciplinary Social and Human Sciences, Kindai University, Shinkamikosaka 228-3, Higashiosaka-shi, Osaka 577-0813, Japan
[14] Centre for Astrophysics, University of Southern Queensland, Toowoomba, Queensland 4350, Australia
[15] Aix-Marseille Université, CNRS, LAM (Laboratoire d'Astrophysique de Marseille) UMR 7326, 13388 Marseille, France

Received 29 December 2017 / Accepted 3 July 2018

ABSTRACT

Context. A group of trans-Neptunian objects (TNOs) are dynamically related to the dwarf planet 136108 Haumea. Ten of them show strong indications of water ice on their surfaces, are assumed to have resulted from a collision, and are accepted as the only known TNO collisional family. Nineteen other dynamically similar objects lack water ice absorptions and are hypothesized to be dynamical interlopers.

Aims. We have made observations to determine sizes and geometric albedos of six of the accepted Haumea family members and one dynamical interloper. Ten other dynamical interlopers have been measured by previous works. We compare the individual and statistical properties of the family members and interlopers, examining the size and albedo distributions of both groups. We also examine implications for the total mass of the family and their ejection velocities.

Methods. We use far-infrared space-based telescopes to observe the target TNOs near their thermal peak and combine these data with optical magnitudes to derive sizes and albedos using radiometric techniques. Using measured and inferred sizes together with ejection velocities, we determine the power-law slope of ejection velocity as a function of effective diameter.

Results. The detected Haumea family members have a diversity of geometric albedos ~0.3–0.8, which are higher than geometric albedos of dynamically similar objects without water ice. The median geometric albedo for accepted family members is $p_V = 0.48^{+0.28}_{-0.18}$, compared to $0.08^{+0.07}_{-0.05}$ for the dynamical interlopers. In the size range $D = 175$–300 km, the slope of the cumulative size distribution is $q = 3.2^{+0.7}_{-0.4}$ for accepted family members, steeper than the $q = 2.0 \pm 0.6$ slope for the dynamical interlopers with $D < 500$ km. The total mass of Haumea's moons and family members is 2.4% of Haumea's mass. The ejection velocities required to emplace them on their current orbits show a dependence on diameter, with a power-law slope of 0.21–0.50.

Key words. Kuiper belt: general – infrared: planetary systems – methods: observational – techniques: photometric

⋆ *Herschel* is an ESA space observatory with science instruments provided by a European-led Principal Investigator consortia and with important participation from NASA.

1. Introduction

Over the past 25 yr, a large number of icy bodies have been discovered orbiting beyond Neptune in the outer solar system. These trans-Neptunian objects (TNOs) are material left behind from the formation of our solar system, and contain a wealth of information on how the planets migrated to their current orbits. In addition, they likely constitute the principal source of short-period comets, through their daughter population, the centaurs (Levison & Duncan 1997; Horner et al. 2004). The dwarf planet 136108 Haumea is one of the largest TNOs. With a volume-equivalent diameter of $D \sim 1600$ km (Ortiz et al. 2017), its size is between the category of Pluto and Eris ($D > 2300$ km; Sicardy et al. 2011) and the other largest TNOs 2007 OR_{10}, Makemake, Quaoar, and Sedna (Ortiz et al. 2012a; Santos-Sanz et al. 2012; Pál et al. 2012, 2016; Braga-Ribas et al. 2013). While mutual collisions have shaped the size distribution of small and moderate sized TNOs (diameter < 50–100 km) larger TNOs have generally not been eroded by disruptive collisions, so their size distribution is thought to reflect the accretion process (Davis & Farinella 1997). Large objects usually experience impact cratering instead of disruptive collisions. However, the large object Haumea may be an exception to this rule as it is hypothesized to be the parent body of the so-far only identified collisional family among TNOs (Brown et al. 2007; Levison et al. 2008b; Marcus et al. 2011). It has a short rotation period of 3.92 h (Rabinowitz et al. 2006) close to the calculated and observed spin breakup limit of TNOs (Leinhardt et al. 2010; Thirouin et al. 2010) as well as a rotationally deformed shape and a ring (Ortiz et al. 2017), which all are unique properties among the $D \geq 1000$ km TNOs. The geometric albedo of Haumea (~0.5) due to water ice is less than the albedos of Pluto and Eris, which have volatile ices, whereas smaller TNOs with measured albedos available in the literature have geometric albedos $\lesssim$0.4 (e.g. Lacerda et al. 2014a). All TNOs with $D \geq 1000$ km for which spectra have been obtained feature methane ice on their surfaces, except Haumea which has only water ice (Barucci et al. 2011, and references cited therein). Spectral modelling suggests a 1:1 mixture of crystalline and amorphous water ice on Haumea's surface and that it is depleted in carbon-bearing materials besides CH_4 compared to most other TNOs (Pinilla-Alonso et al. 2009).

Brown et al. (2007) noted that a group of five TNOs including Haumea that have very deep near-infrared (NIR) water ice absorption features are also dynamically clustered, that is, they have similar proper orbital elements. Ragozzine & Brown (2007) listed objects with low velocities relative to Haumea's supposed collisional location. About one third of them have strong water ice features and so are family members. At that time it was also known that the larger moon Hi'iaka has a strong water ice absorption in its spectrum (Barkume et al. 2006). Brown et al. (2007) proposed that the group of five objects are fragments of Haumea's ice mantle disrupted by a collision with an object 60% of the size of proto-Haumea. Such a collision may have removed ~20% of Haumea's initial mass. To date, most authors have accepted the hypothesis that only those TNOs which (i) are in the dynamical cluster and (ii) have strong water ice absorptions are members of the family. While some other TNOs have water ice absorptions (Brown et al. 2012), they are weaker, and those TNOs are not part of the dynamical cluster. One member of the dynamical cluster is the $D \sim 300$ km TNO 2002 TX_{300} with high geometric albedo of 0.88 (Elliot et al. 2010), which has been identified as one of the Haumea family members as it has strong water ice absorption bands (Licandro et al. 2006). The whole population of TNOs in general has a wide range of colours (e.g. Doressoundiram et al. 2008; Hainaut et al. 2012) but all the Haumea family members show neutral colours. Spectroscopic data is not available for all potential Haumea family members and new techniques to detect water ice signatures with NIR photometry have been developed (e.g. Snodgrass et al. 2010; Trujillo et al. 2011) in order to infer family membership. The number of spectroscopically or photometrically confirmed members is currently ten in addition to Haumea and its two moons Hi'iaka and Namaka (Brown et al. 2007; Ragozzine & Brown 2007; Schaller & Brown 2008; Fraser & Brown 2009; Snodgrass et al. 2010; Trujillo et al. 2011).

The semi-major axes of the orbits of the Haumea family members are $42.0 < a < 44.6$ AU, their orbital inclinations are $24.2° < i < 29.1°$, and their eccentricities are $0.11 < e < 0.17$. For all the members in the dynamical cluster, the orbital elements are $40 < a < 47$ AU, $22° < i < 31°$, and $0.06 < e \leq 0.2$. Haumea has a more eccentric orbit than the rest of the family with $e = 0.20$. It is currently in a 12:7 mean motion resonance with Neptune (Lykawka & Mukai 2007), and Brown et al. (2007) suggest that its current proper orbital elements have changed since the presumed collision event. Lykawka & Mukai (2007) indicated that 19308 (1996 TO_{66}) is in a 19:11 resonance with Neptune but this resonance membership could not be confirmed by later works (e.g. Lykawka et al. 2012). Unless in mean motion resonance, the confirmed family members are in the dynamically hot sub-population of classical Kuiper belt objects (CKBO) according to the Gladman et al. (2008) classification system, but are classified as scattered-extended in the Deep Ecliptic Survey classification system (Elliot et al. 2005). Collisions in the present classical trans-Neptunian belt are very unlikely and the family would probably have been dispersed during the chaotic migration phase of planets if it formed before the dynamically hot CKBOs had evolved to their current orbits as predicted by the Nice model (e.g. Levison et al. 2008a). Based on calculations of collision probabilities, Levison et al. (2008b) showed that over 4.6 Ga a collision leading to the formation of one family is likely if both the colliding objects were scattered-disk objects on highly eccentric orbits, and that it could result in a CKBO-type orbit after the collision.

One of the biggest challenges to the collisional disruption formation mechanism is that the objects with strong water ice features are tightly clustered, having a velocity dispersion clearly smaller (~20–300 ms^{-1}; Ragozzine & Brown 2007) than the escape velocity of Haumea (~900 ms^{-1}). This is unusual for fragments of a disruptive impact (Schlichting & Sari 2009). Various models have been proposed to explain the small velocity dispersion: a grazing impact of two equal-sized objects followed by merger (Leinhardt et al. 2010); disruption of a large satellite of the proto-Haumea (Schlichting & Sari 2009); and rotational fission (Ortiz et al. 2012b). While the collisional models can explain the low velocity dispersion of the canonically defined family members, another possibility is that the family is more extensive than has been assumed based on NIR spectral evidence. A recent review of collisional mechanisms has been presented by Campo Bagatin et al. (2016). They also propose the alternative that Haumea together with its moons was formed independently of the family of objects presumed to form the rest of the Haumea family, that is, that there were two parent bodies on close orbits. The different water ice fractions on the surfaces of Haumea compared to the family average found by Trujillo et al. (2011) would be compatible with this hypothesis. The inverse correlation of size (via its proxy, the absolute magnitude) with the presence of water ice was explained by Trujillo et al. (2011) to be caused by two possibilities: smaller objects

having a larger fraction of ice on their surfaces or smaller objects having a larger grain size.

In order to quantify the albedos and sizes of Haumea family members, we use all available far-infrared observations. Six of the confirmed family members have been observed with the *Herschel* Space Observatory (Pilbratt et al. 2010) and four of them have also *Spitzer* Space Telescope observations. The radiometric results of five confirmed family members 19308 (1996 TO_{66}), 24835 (1995 SM_{55}), 120178 (2003 OP_{32}), 145453 (2005 RR_{43}), and 2003 UZ_{117} are new in this work. We describe these *Herschel* and *Spitzer* observations as well as optical absolute magnitudes in Sect. 2 and present the radiometric analysis in Sect. 3. We discuss the implication to the Haumea family in Sect. 4 and make conclusions in Sect. 5.

2. Observations and auxiliary data

2.1. Herschel observations

The observations of the Haumea family with the *Herschel* Space Observatory were part of the Open Time Key Program "TNOs are Cool" (Müller et al. 2009), which used in total about 400 h of observing time during the Science Demonstration Phase and Routine Science Phases to observe 132 targets. Haumea itself was observed extensively, more than ten hours with two photometric instruments, the Photodetector Array Camera and Spectrometer (PACS) at 70, 100, and 160 μm (Poglitsch et al. 2010) and the Spectral and Photometric Imaging Receiver (SPIRE) at 250, 350, and 500 μm (Griffin et al. 2010). The thermal light curve of the system of Haumea and its moons were analysed by Lellouch et al. (2010) and Santos-Sanz et al. (2017) and the averaged multi-band observations by PACS and SPIRE in Fornasier et al. (2013). Six confirmed Haumea family members were observed by *Herschel* as part of this work (Table 1) using a total of about 12 h. In addition, eight probable dynamical interlopers[1] were analysed in previous works from "TNOs are Cool" and one of them (1999 KR_{16}) has updated flux densities given in Table 1. The previously unpublished *Herschel* observations of the dynamical interloper 1999 CD_{158} are part of this work.

The *Herschel*/PACS observations of the Haumea family were planned in the same way as other observations in the key programme (e.g. Vilenius et al. 2012). The instrument was continuously sampling while the telescope moved in a pattern of parallel scan legs, each 3′ in length[2], around the target coordinates. We had checked the astrometric uncertainty of the coordinates with the criterion that the 3σ positional uncertainty was less than 10″. Each PACS observation (identified by "OBSID") produced a map that was the result of repeating the scan pattern several times. This repetition factor was a free parameter in the planning of the duration of observations. In the beginning of the Routine Science Phase of *Herschel* in the first half of 2010 (Table 1), we used repetition factors of two to three based on detecting thermal emission of an object assuming it has a geometric albedo of 0.08. Later in 2011 we used longer observing time with repetition factors of four to five to take into account the possible high albedo of Haumea family members as indicated by Elliot et al. (2010) for 2002 TX_{300} because higher geometric albedo at visible wavelengths means less emission in the far-infrared wavelengths.

We used the *Herschel* Interactive Processing Environment (HIPE[3], version 9.0 / CIB 2974) to produce Level 2 maps with the scan map pipeline script, with TNO-specific parameters given in Kiss et al. (2014). This script projects pixels of the original frames produced by the detector into pixels of a sub-sampled output map. Each target was observed with the same sequence of individual OBSIDs at two epochs separated by about one day so that the target had moved by 25–50″. We applied background subtraction using the double-differential technique (Kiss et al. 2014) to produce final maps from individual OBSIDs. We used standard aperture photometry techniques to determine flux densities. The uncertainties were determined by implanting 200 artificial sources in the vicinity of the real source and calculating the standard deviation of flux densities determined from these artificial sources. The upper limits in Table 1 are 1σ noise levels of the final map determined by this artificial source technique. The colour corrections were calculated in the same iterative way as in Vilenius et al. (2012) and they amount to a few percent. The uncertainties include the absolute calibration uncertainty, which is 5% in all PACS bands (Balog et al. 2014).

The previously published *Herschel* observations of 1999 KR_{16} (Santos-Sanz et al. 2012) have been re-analysed in this work (Table 1). Santos-Sanz et al. (2012) used the super-sky subtraction method (Stansberry et al. 2008) and reported flux densities of 5.7 ± 0.7/3.5 ± 1.0/4.6 ± 2.2 mJy, which were "mutually inconsistent" as shown in their Fig. 1. In our updated analysis we found out that there was a background source near the target located in such a way that the double-differential technique (Kiss et al. 2014) did not fully remove it. We consider the visit 2 images as contaminated and use only visit 1. Moreover, we consider the 160 μm band an upper limit.

2.2. Spitzer observations

Four members of the Haumea family were observed using the Multiband Imaging Photometer for *Spitzer* (MIPS; Rieke et al. 2004) aboard the *Spitzer* Space Telescope (Werner et al. 2004). These observations utilized MIPS' chop-nod photometric mode using the dedicated chopper mirror and spacecraft slews as nods, and the spectral channels centred at 24 μm (effective monochromatic wavelength: 23.68 μm) and 70 μm (71.42 μm). There is strong spectral overlap between the 70-micron channels of MIPS and PACS.

We reanalysed (Mueller et al., in prep.) the MIPS observations using the methods described by Stansberry et al. (2007, 2008) and Brucker et al. (2009), along with recent ephemeris information. Targets 2002 TX_{300} and 2003 OP_{32} were observed more than once and a background-subtraction method was used to produce combined maps. The individual visits were made within about two days of the first visit of the observed target. Flux densities were determined from the resulting mosaics using aperture photometry. Flux uncertainties were estimated using two techniques, one using a standard sky annulus, one using multiple sky apertures.

None of the Haumea family members were detected by *Spitzer*. Our analysis provides upper flux limits (see Table 2). We provide tighter limits based on new reduction of the data on the non-detection of 2002 TX_{300} than a previous analysis by

[1] Interlopers (as defined by Ragozzine & Brown 2007) belong to the same dynamical cluster as Haumea family members but they lack the spectral features to be confirmed as family members.

[2] The observations in February 2010 were done with a scan leg length of 2.5′.

[3] Data presented in this paper were analysed using "HIPE", a joint development by the *Herschel* Science Ground Segment Consortium, consisting of ESA, the NASA *Herschel* Science Center, and the HIFI, PACS and SPIRE consortia.

Table 1. *Herschel* observations and monochromatic flux densities of six unpublished and two reanalysed targets.

Target	1st OBSIDs of visit 1/2	Dur. (min)	Mid-time	r (AU)	Δ (AU)	α (°)	Flux densities [mJy] 70 μm	100 μm	160 μm
1995 SM_{55}	1342190925/...0994	73.1	2010-Feb-22 11:58	38.62	38.99	1.37	<1.7	<1.7	<2.7
2005 RR_{43}	1342190957/...1033	73.1	2010-Feb-23 00:16	38.73	38.88	1.45	2.6 ± 1.8	4.6 ± 2.4	<2.8
2003 UZ_{117}	1342190961/...1037	109.3	2010-Feb-23 01:07	39.27	39.50	1.41	2.0 ± 1.6	<2.2	<2.3
2003 OP_{32}	1342197669/...7721	75.7	2010-Jun-03 20:31	41.53	41.31	1.39	1.7 ± 1.5	<2.1	<4.1
2002 TX_{300}	1342212764/...2802	188.5	2011-Jan-17 03:46	41.68	41.76	1.36	1.2 ± 1.1	<2.8	<4.1
1996 TO_{66}	1342222430/...2481	188.5	2011-Jun-10 11:25	46.92	47.34	1.14	<1.2	<1.3	<2.9
1999 CD_{158}	1342206024/...6060	150.9	2010-Oct-08 05:01	47.40	47.83	1.09	<1.3	<1.6	<2.1
1999 KR_{16}	1342212814/...3071	188.5	2011-Jan-18 06:14	35.76	36.06	1.51	4.2 ± 1.1[a]	6.9 ± 2.2[a]	<4.5

Notes. Targets 2002 TX_{300} (Lellouch et al. 2013) and 1999 KR_{16} (Santos-Sanz et al. 2012) have been reanalysed and their flux densities updated in this work. OBSIDs are observation identifiers in the *Herschel* Science Archive. The first OBSID of the consecutive OBSIDs/visit are given. Duration is the total duration of the two visits (70 and 100 μm filters were used for half of the duration each), mid-time is the mean UT time, r is the heliocentric distance at mid-time, Δ is the *Herschel*-target distance at mid-time, and α is the Sun-target-*Herschel* phase angle at mid-time (JPL Horizons Ephemeris System; Giorgini et al. 1996). Flux densities are colour-corrected and the 1σ uncertainties include the absolute calibration uncertainty of 5% in all bands. Targets above the horizontal line are confirmed Haumea family members while those below the line are probable dynamical interlopers. [(a)]Differential fluxes from visit 1 only. During visit 2 a background source was near the target location. This background source is close to the edge of the images from visit 1 and could not be properly compensated by the positive and negative images.

Table 2. *Spitzer*/MIPS observations.

Target	PID	Mid-time	r (AU)	Δ (AU)	α (°)	MIPS 24 μm band Dur. (min)	F_{24} (mJy)	MIPS 70 μm band Dur. (min)	F_{70} (mJy)
1995 SM_{55}	55	2006-Feb-18 16:27	38.93	39.03	1.47	16.5	<0.045	22.4	<3.75
1996 TO_{66}	55	2004-Dec-26 10:22	46.40	46.22	1.23	...	...	44.8	<4.66
2002 TX_{300}	3283	2004-Dec-28 02:04	40.98	40.73	1.37	5.3	<0.025	5.6	<5.59
2003 OP_{32}	30081	2006-Dec-07 00:49	41.19	41.15	1.41	57.5	<0.015	33.6	<4.80
1999 KR_{16}	55	2006-Feb-18 05:51	36.73	36.65	1.56	...	...	44.8	<2.24

Notes. PID is the *Spitzer* programme identifier. Observing geometry (heliocentric distance r, *Spitzer*-target distance Δ, and Sun-target-*Spitzer* phase angle α) is averaged over the individual observations. The "Dur." column gives the total observing time (2002 TX_{300} and 2003 OP_{32} had more than one visit). Targets above the horizontal line are confirmed Haumea family members and 1999 KR_{16} is a probable dynamical interloper.

Stansberry et al. (2008); the remaining observations have not been published so far.

2.3. Optical data

In the radiometric method, we simultaneously fit flux densities and absolute magnitude H_V to the model of emitted flux and to the optical constraint, respectively (Eqs. (1) and (2) in Sect. 3.1). Generally, an accurate H_V affects mainly the accuracy of the estimate of geometric albedo and has a weaker effect on the accuracy of the diameter estimate when far-infrared data is available. However, in the case of high-albedo objects the accuracy of the diameter estimate is affected more strongly by the uncertainty in H_V than in the general case.

Due to their large distance, observations of TNOs from the ground or from near Earth are always done at small Sun-target-observer phase angles and a linear phase function is mostly used to derive H_V in the literature. Haumea and four of the confirmed Haumea family members (Table 3) have been observed with dozens of individual exposures at phase angles α in the range $0.3° < \alpha < 1.5°$ (Rabinowitz et al. 2007, 2008) and taking into account and reducing short-term variability due to rotational light curves. These carefully determined phase coefficients of the five objects are between ~0.01 and ~0.1 mag deg^{-1} with a weighted average of 0.066 ± 0.024 mag deg^{-1}. The exact shape of a phase curve depends on scattering properties of the surface and, for example, on porosity and granular structure (Rabinowitz et al. 2008). A typical opposition spike at small phase angles $\alpha \lesssim 0.2°$, compared to extrapolating a linear phase curve, is a brightening of ~0.1 mag (Belskaya et al. 2008, and references cited therein). Such a brightening would mean a relative increase in the value of geometric albedo of ~10%. However, high-albedo objects with a phase curve slope $\gtrsim$0.04 mag deg^{-1} already have an opposition surge that is too wide to allow a narrow spike near zero phase angle (Schaefer et al. 2009). The average of good quality phase slopes of Haumea and its family (Table 3) is greater than the limit of ~0.04 mag deg^{-1} and therefore we have not applied the 0.1 mag brightening of H_V in this work.

The light curve due to rotation changes the optical brightness from the nominal value between individual observations by PACS and MIPS and phasing of optical data with the thermal observations is uncertain, therefore, we quadratically add a light curve effect to the uncertainties of H_V before thermal modelling as explained in Vilenius et al. (2012). This additional uncertainty is explicitly shown with the uncertainty of H_V in Table 3.

For targets lacking a phase curve study in the literature, we determine the linear phase coefficient from combinations of photometric-quality data points when available and/or data from the Minor Planet Center (MPC), which is more uncertain (see Table 4). Since these data have not been reduced for short-term variability due to rotation, we have added an uncertainty to each data point in the way explained above. There is usually no data

Table 3. Absolute magnitudes from detailed phase curve studies as well as light curve properties.

Target	Amplitude (mag)	Period (h)	Single/double peaked	$H_V^{d,e}$ (mag)	Phase coefficient[d] (mag/°)
136108 Haumea	0.320 ± 0.006[i]	3.9154 ± 0.0002[h]	double[h]	0.428 ± 0.011[h]	0.097 ± 0.007
24835 (1995 SM_{55})	0.04 ± 0.02[g]	8.08 ± 0.03[a]	double[g]	4.490 ± 0.030 ± 0.018	0.060 ± 0.027
55636 (2002 TX_{300})	0.05 ± 0.01[b]	8.15[b]	double[b]	3.365 ± 0.044 ± 0.022	0.076 ± 0.029
120178 (2003 OP_{32})	0.14 ± 0.02[g]	4.85[f]	single[g]	4.097 ± 0.033 ± 0.062	0.040 ± 0.022
145453 (2005 RR_{43})	0.06 ± 0.01[c]	7.87[c]	single[c]	4.125 ± 0.071 ± 0.026	0.010 ± 0.016
				Average	0.066 ± 0.024

Notes. Light curve amplitude is the peak-to-valley amplitude, which is taken into account in the error bars of the absolute V-band magnitude H_V from literature when H_V is used as input in the radiometric analysis (see text).
References. [(a)]Sheppard & Jewitt (2003); [(b)]Thirouin et al. (2012); [(c)]Thirouin et al. (2010); [(d)]Rabinowitz et al. (2008); [(e)]Rabinowitz et al. (2007); [(f)]Benecchi & Sheppard (2013); [(g)]Thirouin et al. (2016); [(h)]Rabinowitz et al. (2006); [(i)]Lockwood et al. (2014).

available at very small phase angles. An exception is 1996 TO_{66}, which has also data points at 0.05° and 0.07°. However, these two points are well compatible with a linear trend and the phase slope of 0.20 ± 0.12 mag deg^{-1} is higher than the ∼0.04 mag deg^{-1} limit. Thus, we can assume that there is no narrow non-linear opposition spike.

The phase coefficients derived in this work are compatible within uncertainties with the average TNO β = 0.12 ± 0.06 mag deg^{-1} of Perna et al. (2013), except 2003 SQ_{317} which is discussed below. A more recent work to determine linear phase coefficients of a large sample of TNOs (Alvarez-Candal et al. 2016) found a median value of 0.10 mag deg^{-1} in a double distribution containing a narrow component and a wider one with approximately half of TNOs belonging to each component of the distribution. The maximum value reported was 1.35 mag deg^{-1}. The difference in determining the phase coefficients in this work and in Alvarez-Candal et al. (2016) is that we represent, for each data point, the un-phased light curve contribution due to rotation by an additional increase in the uncertainty of data points, whereas Alvarez-Candal et al. (2016) assume a flat probability distribution between the minimum and maximum of short-term variability. In Table 4, we report phase slopes for seven targets not included in Alvarez-Candal et al. (2016). The five targets that are included in their work are compatible with our results within error bars, but those uncertainties are sometimes relatively large. For 1999 KR_{16} we have a flat phase curve (0.03 ± 0.15 mag deg^{-1}) with N = 5 data points, whereas Alvarez-Candal et al. (2016) has a negative slope (–0.126 ± 0.180 mag deg^{-1}) with N = 4 data points. Whilst their result is formally consistent with zero it includes a large range of negative values, which is difficult to explain based on known physical mechanisms. For 1999 OY_3 we have a shallower slope with N = 3 because we have rejected one outlier data point.

The highest phase slope among our targets is 0.92 ± 0.30 mag deg^{-1} for 2003 SQ_{317} with most of our data points from Lacerda et al. (2014b), who reported a high slope of 0.95 ± 0.41 mag deg^{-1}. They also modelled the high-amplitude light curve of this target and found that it is either a close binary or has a very elongated shape. It should be noted that the six data points used for 2003 SQ_{317} are limited to phase angles 0.6–1.0 deg. If data for lower phase angles become available in the future, it might change the current slope estimate.

For the candidate Haumea family members (membership neither confirmed nor rejected) we use mostly non-photometric quality data from the Minor Planet Center due to the poor availability of high-quality optical data. The light curve amplitudes are sparsely known and V–R colours are not known for these candidate family members. When the light curve amplitude is unknown we assume it to be 0.2 mag based on the finding of Duffard et al. (2009) that 70% of TNOs have an amplitude less than this value. We try to fit a phase curve slope but in four cases the result is not plausible, or not reliable due to limited phase angle coverage. For those cases we use an assumed value for the phase coefficient of β = 0.12 ± 0.06 mag deg^{-1} (Perna et al. 2013). Given the H_V uncertainties of these four targets, using this average value instead of the average of confirmed Haumea family members from Table 3 would have only a minor effect on the derived absolute magnitudes.

3. Analysis

3.1. Thermal modelling

We use the same thermal model approach as in previous sample papers from the "TNOs are Cool" *Herschel* programme (see e.g. Mommert et al. 2012; Vilenius et al. 2014), which is based on the near-Earth asteroid thermal model (NEATM, Harris 1998). We assume that the objects are airless and spherical in shape. Using the few data points at far-infrared wavelenghts, as well as H_V we solve for size, geometric albedo p_V, and beaming factor η in the equations

$$F(\lambda, r, \Delta, \alpha) = \frac{\epsilon(\lambda)}{\Delta^2} \int_S B\left(\lambda, T\left(S, q p_V, \eta, r, \alpha\right)\right) \, \mathrm{d}\mathbf{S} \cdot \mathbf{u}, \quad (1)$$

$$H_V = m_\odot + 5 \log\left(\sqrt{\pi} a\right) - \frac{5}{2} \log\left(p_V S_{\mathrm{proj}}\right), \quad (2)$$

where λ is the reference wavelength of each of the PACS or MIPS bands, r, Δ, and α give the observing geometry at PACS or MIPS observing epoch (heliocentric distance, observer-target distance, and Sun-target-observer phase angle, respectively), Planck's radiation law B is integrated over the illuminated part of the surface of the object, $\mathbf{u}$ is the unit directional vector towards the observer from the surface element d$\mathbf{S}$, q is the phase integral, p_V is the geometric albedo, η is the beaming factor, and spectral emissivity is assumed to be constant ε = 0.9. In the optical constraint Eq. (2) $m_\odot$ is the apparent solar magnitude at V-band (–26.76 ± 0.02 mag; Hayes 1985; Bessell et al. 1998) and a is the distance of one astronomical unit. In NEATM, the non-illuminated part of the object does not contribute any flux and the temperature distribution at points on the illuminated side is $T(\omega) = T_S \cos^{1/4} \omega$, where ω is the angular distance from the

Table 4. Absolute magnitude based on a linear phase curve fit derived in this work.

Target	V ref.	R ref.	N	Phase coeff. (mag/°)	χ^2_r	L.c. Δm_R (mag)	H_V (mag)	V-R (mag)
Confirmed family members								
1996 TO_{66}	5, 7–8, 13–16, 18	6, 17	9	0.20 ± 0.12	1.6	0.26 ± 0.03[2]	4.81 ± 0.08 ± 0.11	0.389 ± 0.043
1999 OY_3	9–10	11, 23	3	0.013 ± 0.079	3.4	0.08[25]	6.61 ± 0.07	0.345 ± 0.046
2005 CB_{79}	…	11–12, MPC	21	0.09 ± 0.08[b]	0.6	0.05 ± 0.02[25]	4.67 ± 0.07	0.37 ± 0.05[11]
2009 YE_7	…	3[a], MPC	20	(aver. Table 3)[d]	0.5	0.06 ± 0.02[25]	4.65 ± 0.15	(assumed)
2003 SQ_{317}	…	11, 26	6	0.92 ± 0.30[b]	1.0	0.85 ± 0.05[26]	6.47 ± 0.30	(assumed)
2003 UZ_{117}	4, 12, 19–20	…	6	0.11 ± 0.11	0.3	0.2[12]	5.23 ± 0.12 ± 0.09	…
Probable dynamical interlopers								
1999 CD_{158}	10, 24	11, 24	4	0.05 ± 0.80	0.1	0.49 ± 0.03[25]	5.35 ± 0.63 ± 0.22	0.520 ± 0.053
1999 KR_{16}	27	17, 21–23	5	0.03 ± 0.15	0.8	0.18 ± 0.04[21]	6.24 ± 0.13 ± 0.08	0.738 ± 0.057
Candidate family members								
1998 HL_{151}	…	MPC	15	0.63 ± 0.50[b]	0.1	(assumed)	7.88 ± 0.39	(assumed)
1999 OK_4	…	MPC	8	(assumed)[c]	0.05	(assumed)	7.69 ± 0.26	(assumed)
2003 HA_{57}	…	MPC	9	(assumed)[c]	0.2	0.31 ± 0.03[25]	8.21 ± 0.25	(assumed)
1997 RX_9	…	1, MPC	11	0.22 ± 0.31[b]	0.2	(assumed)	8.31 ± 0.22	(assumed)
2003 HX_{56}	11	MPC	8	0.41 ± 0.61[b]	0.2	>0.4[25]	7.00 ± 0.56	(assumed)
2003 QX_{91}	…	MPC	5	(assumed)	1.0	(assumed)	7.87 ± 0.67	(assumed)
2000 JG_{81}	3	MPC	4	0.01 ± 0.28	3.9	(assumed)	8.10 ± 0.45	(assumed)
2008 AP_{129}	…	MPC	13	(assumed)	0.5	0.12 ± 0.02[25]	5.00 ± 0.22	(assumed)
2014 FT_{71}	MPC	MPC	2	0.54 ± 0.56[e]	n/a	(assumed)	4.89 ± 0.48	(assumed)

Notes. References to data from literature and databases are listed with N the total number of individual V- or R-band data points, the assumed phase coefficient is the average of TNO phase coefficients: 0.12 ± 0.06 (Perna et al. 2013), χ^2_r is the reduced χ^2 describing the goodness of fit of the linear phase curve, H_V is the absolute V-band magnitude with uncertainties taking into account light curve (L.c.) amplitude Δm_R. The default light curve amplitude is 0.2 mag (Duffard et al. 2009). The light curve uncertainty is added to targets that have *Herschel* data and taken into account as input H_V in thermal modelling. *V–R* colours are from MBOSS-2 (Hainaut et al. 2012) unless otherwise indicated. The assumed *V–R* colour is the average of dynamically hot CKBOs from MBOSS-2: 0.51 ± 0.14. [(a)]Data from SLOAN's *r'* and *g'* bands converted to *V* or *R* band. [(b)]Phase coefficient at *R* band. [(c)]Data inconsistent and would lead to a negative phase coefficient in a free fit. [(d)]Data limited to a narrow phase angle range and would lead to an implausibly high phase coefficient in a free fit. [(e)]Phase coefficient fit using 12 *w*-band data points from MPC in the phase angle range 0.3 < α <1.2. MPC: Minor Planet Center, `http://www.minorplanetcenter.net/iau/lists/TNOs.html`.

References. (1) Gladman et al. (1998); (2) Sheppard & Jewitt (2003); (3) Benecchi & Sheppard (2013); (4) Boehnhardt et al. (2014); (5) Jewitt & Luu (1998); (6) Sheppard (2010); (7) Davies et al. (2000); (8) Gil-Hutton & Licandro (2001); (9) Tegler & Romanishin (2000); (10) Doressoundiram et al. (2002); (11) Snodgrass et al. (2010); (12) Carry et al. (2012); (13) Romanishin & Tegler (1999); (14) Doressoundiram et al. (2005); (15) Barucci et al. (1999); (16) Hainaut et al. (2000); (17) Jewitt & Luu (2001); (18) Boehnhardt et al. (2001); (19) DeMeo et al. (2009), (20) Perna et al. (2010); (21) Sheppard & Jewitt (2002); (22) Trujillo & Brown (2002); (23) Boehnhardt et al. (2002); (24) Delsanti et al. (2001); (25) Thirouin et al. (2016); (26) Lacerda et al. (2014b); (27) Alvarez-Candal et al. (2016).

sub-solar point and T_S is the temperature at the sub-solar point,

$$T_S = \left(\frac{(1 - q p_V) S_\odot}{\epsilon \eta \sigma r^2} \right)^{\frac{1}{4}}. \quad (3)$$

Here $S_\odot$ is the solar constant and σ is the Stefan–Boltzmann constant. For the phase integral, we use an empirical, albedo-dependent relation, $q = 0.336\, p_V + 0.479$, derived from observations of icy moons of giant planets (Brucker et al. 2009). It can be noted that the two fitted parameters in this relation change when new data become available. Brucker et al. (2009) excluded Phoebe and Europa as outliers. After adding Triton (Hillier et al. 1990), Pluto, and Charon (Buratti et al. 2017), there are still two outliers in the data set: Phoebe and Pluto. Consequently, the fitted slope would be steeper. Nevertheless, we use the Brucker et al. (2009) formula to be consistent with previously published results from the "TNOs are Cool" programme.

Some objects may not be compatible with the NEATM assumption of spherical shape. If we have enough information to assume pole orientation and shape, that is, *a*/*b* and *a*/*c*, where *a*, *b*, and *c* are the semi-axes of an ellipsoid ($a > b > c$), then we can calculate the integral in Eq. (1) over the ellipsoid instead of a sphere. The computational details of using ellipsoidal geometry in asteroid thermal models have been presented in literature, for example, by Brown (1985).

We aim to solve area-equivalent effective diameter assuming a spherical shape (D), p_V, and η in Eqs. (1) and (2) in the weighted least-squares parameter estimation sense, where the weights are the squared inverses of the error bars of the measured data points. Upper limits are replaced by a distribution by assigning them values from a half-Gaussian distribution in a Monte Carlo way using a set of 1000 flux density values. This technique was adopted for faint TNOs by Vilenius et al. (2014). The assumptions of this treatment of upper limits are that there is at least one *IR* band where the target was detected and that the upper limits have a similar planned signal-to-noise ratio as the detected band or bands. This was not the case in the PACS 160 μm band for those targets that were not detected

Table 5. Results of radiometric modelling.

Target	Instruments	No. of bands	D (km)	p_V	η	Solution type	Bands included in solution
Haumea[a]	**PACS, MIPS SPIRE**	**7**	**2322x1704x 1026**	**0.51 ± 0.02**	$\mathbf{1.74^{+0.18}_{-0.17}}$	**fixed** D, p_V	**all PACS, MIPS – 70 all SPIRE**
1996TO$_{66}$	**PACS, MIPS**	**4**	**<330**	**>0.20**	**1.74**	**fixed** η	**PACS – 100**
1996 TO$_{66}$	PACS, MIPS	4	<290	>0.27	1.20	fixed η	PACS-100
1995SM$_{55}$	**PACS, MIPS**	**5**	**<280**	**>0.36**	**1.74**	**fixed** η	**PACS – 100**
1995 SM$_{55}$	PACS, MIPS	5	<250	>0.45	1.20	fixed η	PACS-100
2002TX$_{300}$[b]	**PACS, MIPS**	**5**	$\mathbf{323^{+95}_{-37}}$	$\mathbf{0.76^{+0.18}_{-0.45}}$	$\mathbf{1.8^{+0.5}_{-0.9}}$	**fixed** D, p_V	**PACS – 70, PACS – 100**
2003OP$_{32}$	**PACS, MIPS**	**5**	$\mathbf{274^{+47}_{-25}}$	$\mathbf{0.54^{+0.11}_{-0.15}}$	**1.74 ± 0.17**	**fixed** η	**MIPS – 24, PACS – 70, PACS – 100**
2003 OP$_{32}$	PACS, MIPS	5	248^{+32}_{-23}	$0.66^{+0.15}_{-0.14}$	1.20 ± 0.35	fixed η	MIPS-24, PACS-70, PACS-100
2005RR$_{43}$	**PACS**	**3**	$\mathbf{300^{+43}_{-34}}$	$\mathbf{0.44^{+0.12}_{-0.10}}$	**1.74 ± 0.17**	**fixed** η	**all PACS**
2005 RR$_{43}$	PACS	3	268^{+42}_{-26}	$0.55^{+0.13}_{-0.15}$	1.20 ± 0.35	fixed η	all PACS
2003UZ$_{117}$	**PACS**	**3**	$\mathbf{222^{+57}_{-42}}$	$\mathbf{0.29^{+0.16}_{-0.11}}$	**1.74 ± 0.17**	**fixed** η	**PACS – 70, PACS – 100**
2003 UZ$_{117}$	PACS	3	192^{+54}_{-28}	$0.39^{+0.16}_{-0.15}$	1.20 ± 0.35	fixed η	PACS-70, PACS-100
1999KR$_{16}$	**PACS, MIPS**	**4**	$\mathbf{232^{+34}_{-36}}$	$\mathbf{0.105^{+0.049}_{-0.027}}$	**1.20 ± 0.35**	**fixed** η	**MIPS – 70, all PACS**
1999CD$_{158}$	**PACS**	**3**	**<310**	**>0.13**	**1.20 ± 0.35**	**fixed** η	**PACS – 70**

Notes. When different fixed beaming factors have been used, the preferred solution is given in bold. [(a)]Size and geometric albedo from Ortiz et al. (2017); [(b)]diameter from re-analysis of the occultation result of Elliot et al. (2010; see text).

in near-simultaneous PACS 100 μm observations either. Therefore, the 160 μm upper limit is used only in the cases of 2005 RR$_{43}$ and 1999 KR$_{16}$. In the other cases, where this wavelength is ignored, the solution is below the 1σ upper limit at 160 μm. All the *Spitzer*/MIPS flux densities are upper limits (except Haumea itself), and the MIPS 70 μm band observations of confirmed Haumea family members with shorter observation durations than with the more sensitive PACS instrument have been excluded. The MIPS 24 μm upper limit has been included only in the modelling of 2003 OP$_{32}$ although the solution using only PACS bands is very similar to that including also the MIPS 24 μm upper limit. The data sets did not allow us to determine beaming factors and therefore we used a fixed value for η (see Sect. 3.4). An exception is 2002 TX$_{300}$, whose size has been measured via an occultation. This target is discussed in Sect. 3.3. The results of radiometric fits are given in Table 5, where the last column indicates which bands were included in the analysis of the reported solutions, which are shown in Fig. 1. Non-detected targets have been analysed in the same way as in Vilenius et al. (2014): the 2σ flux limit of the most limiting band is used to derive an upper limit for effective diameter (lower limit for geometric albedo). For uncertainty estimates we use the Monte Carlo method of Mueller et al. (2011) with 1000 randomized input flux densities and randomized absolute visual magnitudes as well as randomized beaming factors in the case of fixed-η solutions.

3.2. Haumea

The optical light curve of Haumea has a large amplitude (Rabinowitz et al. 2006), which is indicative of a shape effect. Time-resolved photometry shows a lower-albedo region on its surface, which may cover more than 20% of the instantaneous projected surface area (Lacerda et al. 2008). Lockwood et al. (2014) observed the optical light curve by *Hubble* and were able to resolve the contribution of the primary component excluding the contribution of Haumea's moons. They report a light curve amplitude of 0.320 ± 0.006 mag (valley-to-peak). Using this light curve Lockwood et al. (2014) derived Haumea's size assuming hydrostatic equilibrium, an equator-on viewing geometry, and Hapke's reflectance model (with parameters derived for the icy moon Ariel): a = 960 km, b = 770 km, and c = 495 km for the semi-axes, respectively. Most recently, the shape of Haumea was derived in a more direct way from a stellar occultation (Ortiz et al. 2017): a = 1161 ± 30 km, b = 852 ± 4 km, c = 513 ± 16 km. Furthermore, the new density estimate based on this occultation result indicates that the assumption of hydrostatic equilibrium does not apply in the case of Haumea (Ortiz et al. 2017). The equivalent mean diameter of the projected surface corresponding to the above mentioned ellipsoid is $2a^{1/4}b^{1/4}c^{1/2}$ = 1429 ± 22 km, which is within the uncertainty of the less accurate radiometric spherical-shape size estimate of 1324 ± 167 km (Lellouch et al. 2010). However, a size estimate done by a similar method but using more data points in far-infrared wavelengths gave a significantly smaller size of 1240^{+69}_{-58} km (Fornasier et al. 2013). The geometric albedo of Haumea based on the occultation is p_V = 0.51 ± 0.02 (Ortiz et al. 2017). Since the calculation of the geometric albedo requires the absolute magnitude H_V , Ortiz et al. (2017) used an updated value of H_V for the time of the occultation and assumed a brightness contribution of 11% from the two moons and 2.5% from the ring.

In our further analysis we will use Haumea's beaming factor. It has different values reported in the literature: (i) 1.38 ± 0.71 (Lellouch et al. 2010) based on averaged PACS light curve data combined with a *Spitzer* observation using a NEATM-type radiometric model, (ii) $0.95^{+0.33}_{-0.26}$ (Fornasier et al. 2013) based on a NEATM-type model and averaged data from *Herschel*/PACS as well as observations from *Herschel*/SPIRE and *Spitzer*/MIPS covering a wavelength range from 70 to 350 μm, and (iii) $\eta = 0.89^{+0.08}_{-0.07}$ based on the Lockwood et al. (2014) shape mentioned above and *Spitzer*/MIPS 70 μm light

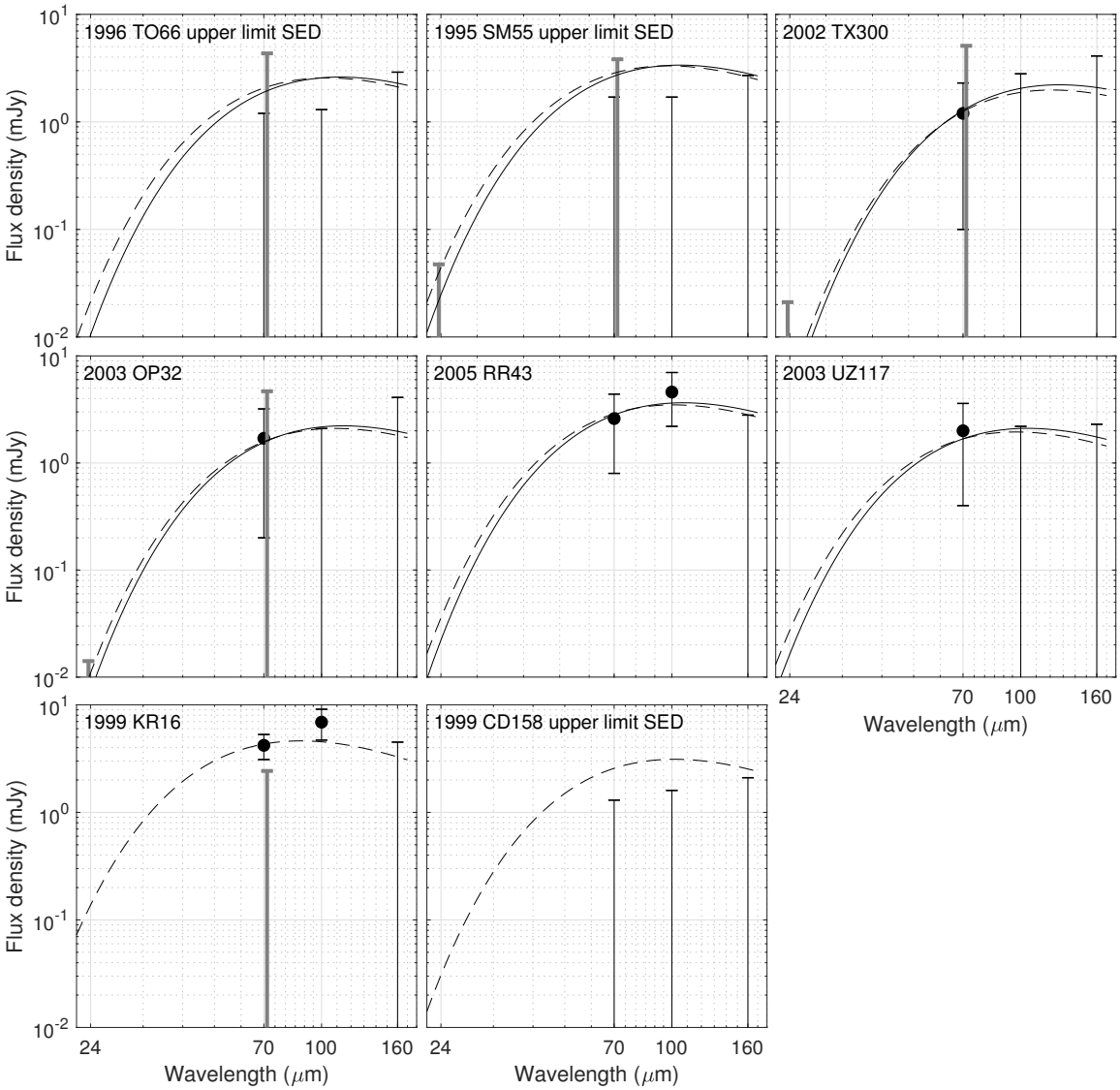

Fig. 1. Modelled flux densities as function of wavelength calculated from solutions in Table 5. Solid lines (when present) are the preferred solutions, dashed lines are fixed beaming factor solutions with $\eta = 1.20$, except for 2002 TX_{300}, where the solid line has $\eta = 1.8$ and the dashed line $\eta = 0.73$. Black data points are PACS data (70, 100, and 160 μm) and grey points are from MIPS (23.68 and 71.42 μm) normalized to the observing geometry of PACS. Error bars are 1σ uncertainties or 1σ upper limits. Upper limit solutions have been calculated for non-detected targets using the 2σ flux density upper limit of the most limiting band (see text).

curve using another thermal model with isothermal temperature at each latitude (as applied by Stansberry et al. 2008) as Haumea is rotating relatively quickly. Because of differences in the radiometric models applied, caution should be taken when comparing the beaming factor of Lockwood et al. (2014) with the other beaming factors. Lellouch et al. (2010) modelled also the PACS light curve of Haumea and determined the beaming factor depending on the assumed pole orientation such that $\eta = 1.15$ if Haumea is equator-on and $\eta = 1.35$ if the equator is at an angle of 15°.

In this work, we have determined the beaming factor η by fixing the semi-axis and geometric albedo using the occultation result and then applying an "ellipsoidal-NEATM" with zero sun-target-observer phase angle (Brown 1985) and far-infrared fluxes of Fornasier et al. (2013) with minor updates. Since the measured fluxes have been obtained by averaging a light curve or by combining at least two separate observations taken several hours apart, we use an average projected size at a rotation of 45° (in a coordinate system where rotation = 0° means that the longest axis is towards the observer). A one-parameter fit with the ellipsoidal thermal model gives $\eta = 1.74^{+0.18}_{-0.17}$. This beaming factor is higher than previous estimates when the accurate size was not available. While Haumea's beaming factor is not unusual for objects at ~50 AU distance from the Sun, there is an observational result that other high-albedo objects ($p_V > 0.20$, see Fig. 2 in Lellouch et al. 2013) have lower beaming factors with the exception of Makemake, whose beaming factor is $\eta = 2.29^{+0.46}_{-0.40}$ (Lellouch et al. 2013) based on *Herschel*/SPIRE data and fixed size and geometric albedo ($p_V \approx 0.77$) from a stellar occultation (Ortiz et al. 2012a). A fast rotation tends to increase the beaming factor η but there are also other effects affecting η such as increasing surface porosity, which lowers its value (Spencer et al. 1989). With $P = 7.7$ h (Thirouin et al. 2010) Makemake is a slower rotator than Haumea.

The beaming factor η is related to the thermal parameter Θ of Spencer et al. (1989), which is the ratio of two characteristic

timescales: the timescale of radiating heat from the subsurface and the diurnal timescale. Figure 5 in Lellouch et al. (2013) shows the beaming factor as a function of the thermal parameter for a spherical object with an instantaneous subsolar temperature of T_0 = 50 K, which is close to the T_0 of Haumea that can be calculated via our Eq. (3) by setting $\eta = 1$. Furthermore, Fig. 4 of Lellouch et al. (2013) shows that the relation between the beaming factor and the thermal parameter does not depend on small differences in the value of T_0 if the thermal parameter is $\Theta \lesssim 10$. However, there is a strong dependence on the aspect angle of the rotation axis and based on the occultation Haumea is seen close to equator-on (Ortiz et al. 2017). The beaming factor derived in this work for Haumea implies a thermal parameter Θ in the order of magnitude of ~3 if there is no surface roughness and up to a factor of approximately two higher in case of high roughness. Thermal inertia Γ is directly proportional to the thermal parameter (Spencer et al. 1989)

$$\Gamma = \Theta \frac{\epsilon \sigma T_0^3}{\sqrt{2\pi}} \sqrt{P}, \quad (4)$$

where P is the rotation period given in Table 3. This estimate gives a thermal inertia of $\Gamma \sim 1$ Jm^{-2} K^{-1} s$^{-\frac{1}{2}}$, which is compatible with the finding of Lellouch et al. (2013) that most high-albedo objects have very low thermal inertias[4]. The value derived in this work is higher than the thermophysical modelling of Santos-Sanz et al. (2017), which indicates that Haumea's thermal inertia is <0.5 Jm^{-2} K^{-1} s$^{-\frac{1}{2}}$ and probably as low as <0.2 Jm^{-2} K^{-1} s$^{-\frac{1}{2}}$. Santos-Sanz et al. (2017) used thermal light curves observed by *Herschel* as well as the shape model and geometric albedo estimate available before the results from the occultation were analysed. Sophisticated thermophysical modelling using the occultation size and shape as well as contributions from the moons, the ring, and a dark spot on Haumea is beyond this work and will be analysed separately (Müller et al., in prep.). The observational result of a lack of high beaming factors of high-albedo objects mentioned earlier is reflected also onto thermal inertias inferred from measured beaming factors and rotational periods: high values of thermal inertia are excluded for high-albedo objects (see Fig. 7 in Lellouch et al. 2013). In addition to Haumea, another moderate to high-albedo TNO that has a value of thermal inertia determined via thermophysical modelling is Orcus. Using *Herschel* observations its thermal inertia has been determined to be $0.4 < \Gamma < 2.0$ Jm^{-2} K^{-1} s$^{-\frac{1}{2}}$ (Lellouch et al. 2013). Orcus has a geometric albedo of $p_V \approx 0.23$ and a beaming factor of $0.97^{+0.05}_{-0.02}$ (Fornasier et al. 2013). Haumea's thermal inertia estimated in this work is compatible with the thermal inertia determined for Orcus although its beaming factor is lower than that of Haumea. With its light curve period of ~10 h (Thirouin et al. 2010), Orcus is a much slower rotator than Haumea but this difference is not enough to explain the difference in beaming factors. Orcus is likely to have a surface with more roughness than that of Haumea.

3.3. Occultation target 2002 TX_{300}

Target 2002 TX_{300} was observed both by *Herschel* and *Spitzer*, but only the PACS/70 μm band gives a weak detection while the other four bands give upper limits. Although Lellouch et al. (2013) reported a three-band detection (all having signal-to-noise ratio <3), after an updated data reduction the PACS 100 and 160 μm bands are now considered upper limits. The *Spitzer* observations of 2002 TX_{300} were of very short duration (Table 2) compared to the *Herschel* observations. We have ignored the *Spitzer* and PACS/160 μm data because those upper limits do not constrain the solution. A floating-η solution that would be compatible with the optical constraint (Eq. (2)) is not possible in the physical range of the beaming factor: $0.6 \leq \eta \leq 2.65$ (limits discussed in Mommert et al. 2012 and Lellouch et al. 2013). However, for this target there is an independent size estimate available from a stellar occultation event in 2009.

The observations of the occultation event of 2002 TX_{300} by several stations resulted in two useful chords. The diameter assuming a circular fit is 286 ± 10 km (Elliot et al. 2010). While the occultation technique may give very accurate sizes of TNOs, it should be noted that in the case of 2002 TX_{300} the result is based on two chords as a reliable elliptical shape fit would require at least three chords. In addition, the mid-times of the occultations reported by the observing stations at Haleakala and Mauna Kea differ by 31.056 s (Table 1 in Elliot et al. 2010). Such an offset, if real, would be compatible with a hypothesis that the two chords are from two separate objects, that is, that 2002 TX_{300} could be a binary. Elliot et al. (2010) mention that one of the chords had to be shifted by 32.95 s to get them aligned for a circular fit (fit parameters were radius, centre position in the sky plane relative to the occulted star, and timing offset). The two-chord occultation and a large timing uncertainty imply a larger uncertainty also in the adopted effective size estimate. The actual shape of an object the size of 2002 TX_{300} may differ from a spherical one since self-gravity is not strong enough for an icy $\lesssim$400 km object to result in a sphere-like shape. The optical light curve is double-peaked which indicates a shape effect. If we assume a Maclaurin spheroid with a rotation period of 8.15 h and a uniform density of 1.0 g cm^{-3} , the axial ratio a/c would be 1.27 according to the figure of equilibrium formalism. This ratio is even larger for lower densities. An ellipsoidal fit with $a/c \sim 1.3$ would give a major axis of 363 km, a minor axis of 289 km, and an effective diameter of 323 km, which is 13% more than the circular fit would give. Even larger effective diameters would result if one of the chords is moved arbitrarily within the timing shift.

The geometric albedo is calculated from the occultation size via absolute magnitude H_V. In this work (see Table 3), we use H_V = 3.365 ± 0.044 mag based on a phase curve study (Rabinowitz et al. 2008), which is different from the H_V used by Elliot et al. (2010; ≈3.48). Using the Elliot et al. (2010) size for a circular fit and the Rabinowitz et al. (2008) absolute magnitude results in a very high geometric albedo of 0.98 ± 0.08. This is higher than the geometric albedo of 0.88 ± 0.06 reported by Elliot et al. (2010) for a circular fit[5] but is within their extended error bar when uncertainty due to possible elliptical fits is taken into account. A geometric albedo of $p_V = 0.98$ would be the highest value among TNOs and similar to that of the dwarf planet Eris ($0.96^{+0.09}_{-0.04}$; Sicardy et al. 2011).

In this work we adopt the above mentioned elliptical solution based on $a/c = 1.3$ and use 323 km as the effective diameter. The lower uncertainty limit is estimated as the difference of this size and the circular solution. The upper uncertainty limit is

[4] The average thermal inertia of TNOs and centaurs, without restricting geometric albedo, is (2.5 ± 0.5) Jm^{-2} K^{-1} s$^{-\frac{1}{2}}$ and the thermal inertia decreases to ~0.5 Jm^{-2} K^{-1} s$^{-\frac{1}{2}}$ for high-albedo objects (Lellouch et al. 2013).

[5] Elliot et al. (2010) increased the upper albedo uncertainty to take into account possible elliptical fits (based on $\Delta m_R = 0.08$ mag) so that the final geometric albedo was $0.88^{+0.15}_{-0.06}$.

challenging to estimate from the occultation data alone. Here, we use the fact that 2002 TX_{300} is close to the detection limit of *Herschel* observations. If the PACS/70 μm data point is interpreted as an upper limit then using the 2σ flux limit as explained in Sect. 3.1 and a conservative high beaming factor we get an upper limit of effective diameter: 418 km. Thus, our new size estimate for 2002 TX_{300} is 323^{+95}_{-37} km and geometric albedo estimate $p_V = 0.76^{+0.18}_{-0.45}$. This geometric albedo is higher but within the large uncertainty compared to Haumea's $p_V = 0.51 \pm 0.02$ (Ortiz et al. 2017).

Using fixed estimates of diameter and geometric albedo in the thermal modelling we can fit the beaming factor. The same approach was used by Lellouch et al. (2013). The new size and geometric albedo estimates given above result in a beaming factor of $\eta = 1.8^{+0.5}_{-0.9}$. This is higher, but compatible within error bars, compared to an earlier result by Lellouch et al. (2013): $\eta = 1.15^{+0.55}_{-0.74}$, which is based on the smaller size and higher geometric albedo reported by Elliot et al. (2010) as well as on an earlier version of flux densities from *Herschel*. For comparison, using the same size estimate of Elliot et al. (2010) and geometric albedo of $p_V = 0.98$ results in a beaming factor of $\eta = 0.73$ using updated *Herschel* fluxes (see also Fig. 1).

3.4. Fixed-η fits

Fixed-η solutions were used when floating-η fits failed. Most of the TNO literature has used the default value $\eta = 1.20 \pm 0.35$ (Stansberry et al. 2008) based on a sample of TNOs of various dynamical classes observed by *Spitzer* where CKBOs were under-represented. Based on a sample of 13 CKBOs observed by *Herschel* and/or *Spitzer,* Vilenius et al. (2014) derived an average of $\eta = 1.45 \pm 0.46$. A larger sample of 85 objects observed by *Herschel* and *Spitzer* representing various dynamical classes gave a mean value of $\eta = 1.175 \pm 0.45$ (Lellouch et al. 2017).

As mentioned in Sect. 3.1, the data quality did not allow a floating-η solution for most targets. Only Haumea and 2002 TX_{300} have a beaming factor determined but the latter was weakly detected only at one thermal band (see Table 1) and has large error bars, which cover most of the physically plausible range of beaming factor values. Since the beaming factor depends on surface properties and heliocentric distance (e.g. Lellouch et al. 2013), we do not have a reliable average η for the Haumea family. In this work we adopt the value of Haumea from the one-parameter fit using the occultation size and albedo as explained in Sect. 3.2, but approximate the asymmetric uncertainties with a symmetric Gaussian distribution in further analysis: $\eta = 1.74 \pm 0.17$. We have adopted this value in our fixed-η fits for confirmed family members (2003 OP_{32}, 2005 RR_{43}, 2003 UZ_{117}, and upper limits of 1996 TO_{66} and 1995 SM_{55}), but show also the results based on the canonical default value $\eta = 1.20 \pm 0.35$ in Table 5. The rotational periods of 2003 OP_{32}, 2005 RR_{43}, and 2003 UZ_{117} have been measured and we can estimate the value of their thermal parameters (Eq. (4)) assuming a value for the thermal inertia. Plausible values are $1.0 < \Gamma < 3.0$ J m^{-2} K^{-1} s$^{-\frac{1}{2}}$ if the thermal inertias of these three objects do not differ significantly from that of Haumea's or the average thermal inertia (see Sect. 3.2). With this range of thermal inertia, the thermal parameter is $2.2 < \Theta < 8.4$ for the three objects. Therefore, a beaming factor value of $\eta \approx 1.74$ is possible for these three objects. We continue to use the default value of the beaming factor 1.20 ± 0.35 for the two moderate-albedo probable dynamical interlopers (1999 KR_{16} and 1999 CD_{158}) modelled in this work, as the probable dynamical interlopers are in a different cluster in a colour-albedo diagram (see Fig. 2 in Lacerda et al. 2014a) and thus probably do not share the surface properties of Haumea family members.

3.5. Comparison with earlier results

Four of the family members, in addition to Haumea, have been observed by *Spitzer*. Based on upper limits at two *Spitzer*/MIPS bands, Brucker et al. (2009) reported 1σ limits for 2002 TX_{300} as $D < 210$ km and $p_V > 0.41$. As discussed in Sect. 3.3, the size of this object, based on a stellar occultation, is larger (Table 5) than the 1σ upper limit by *Spitzer*. The other family members do not have published *Spitzer* results (except Haumea). Altenhof et al. (2004) observed 1996 TO_{66} and 1995 SM_{55} with the 30 m telescope of the Institute for Radio Astronomy in the Millimeter Range (IRAM) at 1.2 mm wavelength. The non-detections gave limits (Grundy et al. 2005) 1996 TO_{66}: $D < 902$ km, $p_R > 0.033$ and 1995 SM_{55}: $D < 704$ km, $p_R > 0.067$. The results of this work give more constraining limits: both targets are smaller than previous limits and have moderate to high albedos (Table 5).

Herschel results of the probable dynamical interloper 1999 KR_{16} have been published by Santos-Sanz et al. (2012). After significant flux updates at 100 and 160 μm (see Sect. 2.1) as well as a fainter H_V, the size estimate is 9% smaller (232^{+34}_{-36} km compared to the previous 254 ± 37 km) but the two results are within each others uncertainties. Geometric albedo is now slightly lower ($p_V = 0.105^{+0.049}_{-0.027}$) than in Santos-Sanz et al. ($p_R = 0.204^{+0.070}_{-0.050}$, which corresponds to a V-band albedo of $p_V \approx 0.14$ using the V–R colour from Table 4).

4. Sample results and discussion

Thirty-five TNOs were identified by Ragozzine & Brown (2007) as potential Haumea family members based on their orbital dynamics and velocities with respect to the centre of mass of the collision, which is approximated by the orbit of Haumea before diffusion under the influence of the 12:7 mean-motion resonance with Neptune. Tables 6 and 8 give the albedos and diameters of the Haumea family members and of probable dynamical interlopers that have measurements relevant to assessing their membership in the family. Table 7 summarizes ejection velocities for dynamically similar TNOs that lack any such data, and so are candidates for membership. The ejection velocities in Tables 6 and 7 may be systematically uncertain for the ensemble of objects, but do reflect the rank order, from slowest to largest ejection velocity (Ragozzine & Brown 2007).

The ejection velocities of 2008 AP_{129}, 2009 YE_7, and 2014 FT_{71} have been calculated by simulations in this work. These results are based on 50 Myr-averaged orbital elements for both the observed orbits and the orbits of test particles in simulated clouds. We considered the nominal orbit plus two orbits with 3σ uncertainties in a–e space and required the clouds of test particles to cover the three orbits in order to determine the minimum ejection velocity of the cloud of test particles. In the case of 2014 FT_{71} the nominal orbit and one other orbit have been influenced by the 7:4 mean motion resonance with Neptune, whereas one orbit is not influenced by this resonance and resulted in a significantly higher ejection velocity of 178 ± 2 m s^{-1} than our preferred result of 30 ± 1 m s^{-1}.

4.1. Size and albedo distributions

We have constructed a combined probability density distribution of geometric albedos based on the few measured targets. The asymmetric uncertainties have been taken into account using the

Table 6. Diameters and albedos of confirmed Haumea family members.

Name	$\Delta v_{\rm min}$ (m s^{-1})	H_2O reference	Thermal data	Diameter (km)	Geometric albedo	Size/albedo reference
136108 Haumea (2003 EL_{61})	323.5	Brown et al. (2007)	(S+H)	$2322 \times 1704 \times 1026$	0.51 ± 0.02	O17
Hi'iaka	...	Barkume et al. (2006)	...	$383^{+74\ a}_{-113}$	default	TW
Namaka	...	Fraser & Brown (2009)	...	193^{+48a}_{-65}	default	TW
19308 (1996 TO_{66})	24.2	Brown et al. (1999)	(S+H)	210^{+40a}_{-62}	default	TW
24835 (1995 SM_{55})	149.7	Brown et al. (2007)	(S+H)	243^{+46a}_{-71}	default	TW
55636 (2002 TX_{300})	107.5	Licandro et al. (2006)	S+H	323^{+95}_{-37}	$0.76^{+0.18}_{-0.45}$	TW, E10[b]
86047 (1999 OY_3)	292.8	Ragozzine & Brown (2007)	...	91^{+17a}_{-27}	default	TW
120178 (2003 OP_{32})	123.3	Brown et al. (2007)	S+H	274^{+47}_{-25}	$0.54^{+0.11}_{-0.15}$	TW
145453 (2005 RR_{43})	111.2	Brown et al. (2007)	H	300^{+43}_{-34}	$0.44^{+0.12}_{-0.10}$	TW
308193 (2005 CB_{79})	96.7	Schaller & Brown (2008)	...	224^{+37a}_{-48}	default	TW
386723 (2009 YE_7)	85[c]	Trujillo et al. (2011)	...	226^{+40a}_{-50}	default	TW
2003 SQ_{317}	148.0	Snodgrass et al. (2010)	...	98^{+20a}_{-24}	default	TW
2003 UZ_{117}	66.8	Schaller & Brown (2008)	H	222^{+57}_{-42}	$0.29^{+0.16}_{-0.11}$	TW

Notes. [(a)]Inferred using geometric albedo of $p_V = 0.48^{+0.28}_{-0.18}$. $\Delta v_{\rm min}$ (from Ragozzine & Brown 2007 unless otherwise indicated) is the minimum of four possible solutions of velocity relative to the collision location's orbit in a calculation where the information about the original orbital angles Ω, ω, and M has been lost. References to first detection of water ice confirming family membership, sources of thermal data: S for *Spitzer* Space Telescope and H for *Herschel* Space Observatory (the parentheses indicate that thermal data were not used in the size/albedo solution shown in this table). O17 = Ortiz et al. (2017), TW = This work, E10 = (Elliot et al. 2010). [(b)]The result of 2002 TX_{300} is from an occultation event re-analysed in this work (see Sect. 3.3). [(c)]This work.

Table 7. Candidate Haumea family members (membership neither confirmed nor rejected).

Target	$\Delta v_{\rm min}$ (m s^{-1})	Class
1998 HL_{151}	142.5	CKBO
1999 OK_4	161.5	CKBO
2003 HA_{57}	214.3	Plutino
1997 RX_9	306.1	CKBO
2003 HX_{56}	363.2	CKBO
2003 QX_{91}	222.0[a]	Res 7:4[b]
130391 (2000 JG_{81})	235.1[a]	Res 2:1[b]
315530 (2008 AP_{129})	107±2[c]	CKBO
2014 FT_{71}	30±1[c]	CKBO[c,d]

Notes. Minimum velocity relative to the collision locations's orbit $\Delta v_{\rm min}$ (Ragozzine & Brown 2007) as in Table 6. Dynamical class is according to the Gladman system (Gladman et al. 2008). [(a)]$\Delta v_{\rm min}$ calculated using adjusted proper elements while conserving the proper Tisserand parameter (Ragozzine & Brown 2007). [(b)]Information about resonant orbits from Volk & Malhotra (2011). [(c)]This work. [(d)]Influenced by 7:4 mean motion resonance.

approach of Mommert (2013). Instead of having two tails from a normal distribution, which would create a discontinuity in case of asymmetric error bars, we use a log-normal distribution[6]. The combined geometric albedos (Fig. 2) of four Haumea family members that have measured geometric albedos (from Table 5) have a median[7] of $p_V = 0.48^{+0.28}_{-0.18}$ using the fixed-η solutions based on Haumea's beaming factor for 2003 OP_{32}, 2005 RR_{43}, and 2003 UZ_{117} (the geometric albedo of 2002 TX_{300} is derived from a stellar occultation) and $p_V = 0.58^{+0.27}_{-0.21}$ if the canonical beaming factor is used instead.

We have measured sizes for four confirmed family members (other than Haumea). For the other family members, absolute visual magnitudes are available. The size distribution of the Haumea family, excluding Haumea (Fig. 3), is constructed in a statistical way by using measured size values when available and otherwise by assigning an albedo from the distribution shown in Fig. 2 and using the absolute visual magnitudes H_V (Table 4). Size distributions are formed 50 000 times so that each measured or inferred size may vary according to its error bar. The slope parameter[8] in the size range 175–300 km is $q = 3.2^{+0.7}_{-0.4}$. All the measured effective diameters are >150 km and the decrease of the slope below this size may be due to an incomplete sample in the size bins <150 km (see the lower panel of Fig. 3) as only two confirmed family members (see Table 6) have size estimates <100 km based on the assumed albedo. If instead of using the sizes and albedo distribution based on the fixed-η value of 1.74 we use solutions based on the canonical value of 1.20 (see Table 5 and Fig. 2), then the slope is steeper

[6] If 63.8% of albedo values in a normal distribution are located within $[p_V - \sigma^-_{p_V}, p_V + \sigma^+_{p_V}]$, where $\sigma^-_{p_V}$ and $\sigma^+_{p_V}$ are the asymmetric uncertainties, then the equivalent amount is located within $[p_V/\exp(\sigma), p_V \exp(\sigma)]$ in a log-normal distribution with shape parameter σ. The shape parameter is determined by setting $p_V + \sigma^+_{p_V} = p_V \exp(\sigma)$ or $p_V - \sigma^-_{p_V} = p_V/\exp(\sigma)$; for practical implementation, see Appendix B.2.2 in Mommert (2013).

[7] The error bars of this median are calculated by finding the p_V points of the c.d.f. of geometric albedo where the value is $\frac{1-\mathrm{erf}(1/\sqrt{2})}{2}$ and $\frac{1+\mathrm{erf}(1/\sqrt{2})}{2}$, for the lower and upper uncertainties, respectively.

[8] We determine the size distribution $N(>D) \propto D^{1-q}$.

Table 8. Diameters and geometric albedos of probable dynamical interlopers of the Haumea family.

Name	Diameter (km)	Geometric albedo	Ref.	Cause of exclusion
1996 TR_{66}	...	...		NIR colours
1999 KR_{16}	232^{+34}_{-36}	$0.105^{+0.049}_{-0.027}$	(1)	Very red
2002 AW_{197}	768^{+39}_{-38}	$0.112^{+0.012}_{-0.011}$	(3)	NIR spectra
1999 RY_{215}	263^{+29}_{-37}	$0.0325^{+0.0122}_{-0.0065}$	(3)	(J-H_S) colour
Salacia	901 ± 45	0.044 ± 0.004	(4)	NIR spectra
Makemake	1430 ± 9	0.77 ± 0.03	(2)	Methane ice
1998 WT_{31}	...	...		Red slope
2005 UQ_{513}	498^{+63}_{-75}	$0.202^{+0.084}_{-0.049}$	(3)	Red slope
1996 RQ_{20}	...	...		Very red
1999 CD_{158}	<310	>0.13	(1)	Very red
1999 OH_4	...	...		NIR colours
2000 CG_{105}	...	...		NIR colours
2001 FU_{172}	...	...		Red slope
2001 QC_{298}	303^{+29}_{-32}	$0.063^{+0.029}_{-0.018}$	(3)	(J-H_S) colour
2002 GH_{32}	<230	>0.13	(3)	Very red
2003 TH_{58}	...	...		(J-H_S) colour
2004 PT_{107}	400^{+45}_{-51}	$0.033^{+0.011}_{-0.007}$	(3)	(J-H_S) colour
2005 GE_{187}	...	...		(J-H_S) colour
2010 KZ_{39}	...	...		NIR colours

Notes. Diameter is given only if measured by thermal radiometric techniques or by occultations. The upper/lower limits of size/albedo are based on 2σ flux density limits of the most constraining wavelength band. The reason used in the literature (e.g. Snodgrass et al. 2010) to reject a target as a family member is given in the last column.
References. (1) This work, (2) Ortiz et al. 2012a, (3) Vilenius et al. 2014, (4) Fornasier et al. 2013.

$q = 3.8^{+0.9}_{-0.5}$ although it is within the uncertainties of the preferred solution. However, sizes are generally smaller and geometric albedos higher when the canonical beaming factor has been used and there are less simulated objects in the 300 km size bin. Considering the size range 150–275 km (i.e. excluding the last size bin) gives a result that is similar to the nominal solution: $q = 3.1^{+0.7}_{-0.4}$.

The slope of the size distribution obtained here can be compared with the slope of dynamically hot CKBOs since most of the family members and probable dynamical interlopers belong to that class. The large end of the size distribution of dynamically hot CKBOs is $q = 4.3 \pm 0.9$ (Vilenius et al. 2014) turning into a shallower slope of $q = 2.3 \pm 0.1$ in the size range 100–500 km. We have also determined the size distribution of <500 km probable dynamical interlopers from Table 8 (using average geometric albedo of dynamically hot CKBOs from Vilenius et al. (2014) and H_V from MPC when no measured size available): $q = 2.0 \pm 0.6$, which is compatible with the slope parameter of the general hot CKBO population. Comparing the two above-mentioned slope parameters to those determined for the Haumea family ($q \sim 3$) indicates that the family has a slope that is steeper than the background population of dynamically hot CKBOs in the same size range.

There are different models for the slope of the size distributions of collisional fragments in the literature. The value determined in this work is approximately compatible with the classical slope of –2.5 (Dohnanyi 1969; Carry et al. 2012), which corresponds to $q = 3.5$ in our definition of the slope parameter.

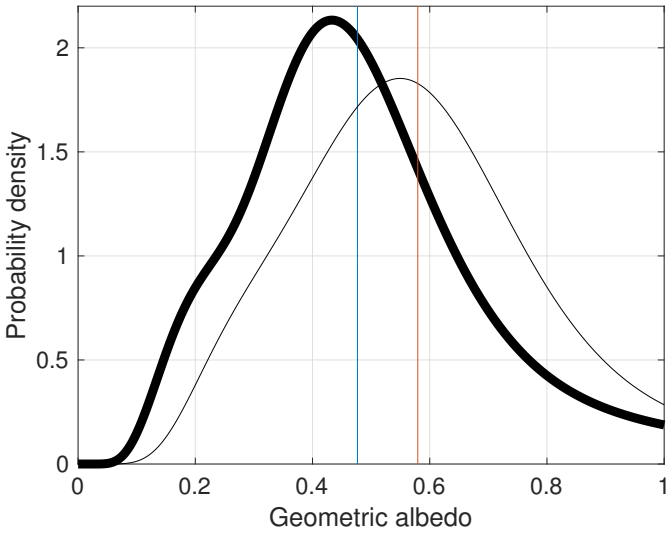

Fig. 2. Combined probability density distribution of geometric albedos of confirmed Haumea family members 2002 TX_{300}, 2003 OP_{32}, 2005 RR_{43}, and 2003 UZ_{117}. The thick line is the albedo distribution assuming the solutions based on the beaming factor value $\eta = 1.74 \pm 0.17$ for 2003 OP_{32}, 2005 RR_{43}, and 2003 UZ_{117} and the thin line assuming the solutions with the canonical beaming factor value $\eta = 1.20 \pm 0.35$. The median values of the two distributions are $p_V = 0.48^{+0.28}_{-0.18}$ (blue vertical line indicates the median) for the preferred solutions and $p_V = 0.58^{+0.27}_{-0.21}$ (red vertical line) assuming the canonical beaming factor.

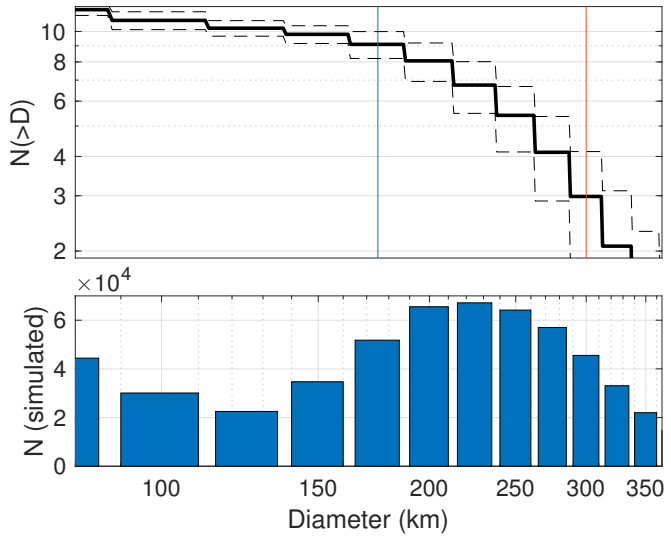

Fig. 3. Combined statistical distribution of sizes (measured if available, otherwise inferred from the albedo distribution and H_V) of confirmed Haumea family members, including the moons. The bin size is 25 km. The size range 150–300 km for which the slope parameter is determined is indicated by the blue and red vertical lines. The *lower panel* shows the size histogram of 50 000 randomly generated objects (see text).

4.2. Albedo and family membership

The albedos and diameters of the TNOs assumed to be dynamical interlopers in the Haumea family are given in Table 8. The table also briefly summarizes the rationale for excluding each object from inclusion as a true member of the collisional family. The albedo values are an independent data set that bears on the question of family membership. Excluding Makemake and Salacia, each of comparable size to Haumea and therefore

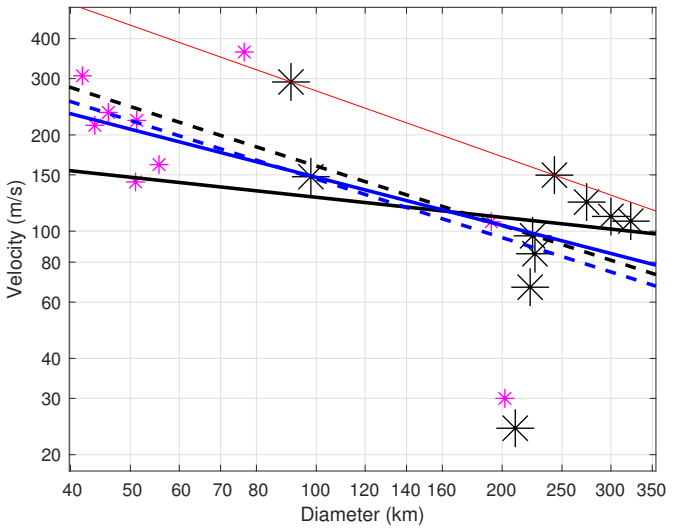

Fig. 4. Distribution of ejection velocities. The large black dots are confirmed Haumea family members (Table 6) and the magenta dots are candidate family members (Table 7). The dashed black line is a fit to all confirmed family members ($\gamma = 0.62$); the solid black line is a fit to the same data but excluding the minimum and maximum velocities ($\gamma = 0.21$). The red line is a limiting case of the confirmed family members ($\gamma = 0.68$). The dashed blue line is a fit to all confirmed and candidate family members ($\gamma = 0.61$) and the solid blue line a fit to the same data excluding minimum and maximum velocities ($\gamma = 0.50$).

inconsistent with the assumption that Haumea itself defines the centre of mass for the collisional family, the median geometric albedo for these objects is $0.08^{+0.07}_{-0.05}$. Most of the objects in Table 8 are dynamically hot CKBOs, and their average albedo is consistent with the average albedo of those objects, $p_V = 0.085^{+0.084}_{-0.045}$ (Vilenius et al. 2014). As discussed in Sect. 4.1, the average albedo measured for the four accepted family members is 0.48, much higher than for the objects in Table 8. This suggests that these objects do not have albedos similar to those of the accepted family members (although the sample sizes, six interlopers and four family members, are very small). Of the objects in Table 8, only the hot CKBO 2005 UQ_{513} has an unusually high albedo, and its albedo is significantly higher than the average for hot CKBOs in general. Our results for 1999 CD_{158} and 2002 GH_{32} suggest that they may also have high albedos. Table 8 gives the 2σ lower limits on albedo and upper limits on size (i.e. the probability that the geometric albedo is <0.13 is ≈4.6%). In summary, albedo measurements for objects previously identified as dynamical interlopers seem to support that identification in general, but suggest that three of them may have unusually high albedos, and further investigation may be warranted. It is unfortunate that there is not more data constraining the albedos and diameters of both the interlopers and the family members.

The Haumea family members have significantly higher albedos than the averages of scattered disk, detached, or cold CKBOs, which are the dynamical classes with the highest average albedos (Santos-Sanz et al. 2012; Vilenius et al. 2014). For mid-sized TNOs, such as Haumea family members, the high albedo surface indicates lack of hydrocarbons, which would have produced a darker and redder surface over long periods of exposure to space weathering (Brown 2012). This is compatible with the collisional hypothesis, which states that the fragments are high-albedo water ice pieces from the mantle of proto-Haumea. In a colour-albedo plot the Haumea family members, with their high albedos, are distinct from the probable dynamical interlopers, which are more widely spread in the colour-albedo plot of Lacerda et al. (2014a, Fig. 2).

4.3. Mass and ejection velocity

The masses of Haumea's moons Hi'iaka and Namaka are $(20.0 \pm 1.2) \times 10^{18}$ and $(2.0 \pm 1.6) \times 10^{18}$ kg (Ragozzine & Brown 2009; Ćuk et al. 2013). For the other family members we estimate masses assuming bulk densities of 1 g cm^{-3}. The confirmed members would constitute approximately 2.4% of the mass of Haumea (using sizes from Table 6 when no mass or size measurement available). The largest family member, the moon Hi'iaka, would alone constitute 21% of the mass of the family excluding Haumea and the five largest family members would be more than half of the total mass of the family (excluding Haumea). Using the alternative radiometric solutions of Table 5 and the lower median geometric albedo results in a mass estimate of 2.0%. If all the candidate family members in Table 7 were be confirmed, they would constitute ∼0.2% of Haumea's mass.

The scenarios in which the proto-moon of Haumea underwent fission to produce a family presented by Ortiz et al. (2012b) require that the mass of the moons and the family members is less than 20% of Haumea's mass. Ortiz et al. (2012b) had only one measured albedo available (2002 TX_{300}) and they used a default geometric albedo of 0.6 for other family members. Our new observations give more confirmation in using a high albedo and our new mass estimate of the family is compatible with the mass ratio assumption used by Ortiz et al. (2012b). Our mass estimate of 2.4% does not exclude the formation mechanisms by disruption of a large satellite of proto-Haumea (Schlichting & Sari 2009), which predicts an upper mass ratio limit of 5%. The mechanism proposed by Leinhardt et al. (2010), where two equal-sized objects merge, predicts a mass ratio of 4–7% (Volk & Malhotra 2012), which is higher than our current estimate.

The ejection velocity of a fragment and its mass are related via a power law. Assuming a constant density for all family members, this relation may be written in terms of the diameter as (Lykawka et al. 2012) $v_e \propto D^{-\gamma}$, where v_e is the ejection velocity and the power-law slope γ is $\lesssim$0.5 (Zappala et al. 2002). Figure 4 shows a fit to effective diameters and velocities from Table 6. A fit using confirmed family members gives $\gamma = 0.62$, which is slightly larger than the upper limit of plausible values. Lykawka et al. (2012) and references cited therein note that there is often large scatter in the ejection velocity values and large ratios of maximum-to-minimum values. Therefore, another fit is made by ignoring the minimum and maximum velocities (1996 TO_{66} and 1999 OY_3). This gives a lower value of $\gamma = 0.21$. We have repeated the fit with an extended data set including all the candidate family members (Table 7 and inferred sizes using the geometric albedo distribution of the Haumea family). The extended data set gives $\gamma = 0.61$ for all data and $\gamma = 0.50$ when minimum and maximum velocities are excluded (1996 TO_{66} and 2003 HX_{56}). In the above calculations, we used absolute visual magnitudes and an assumed geometric albedo of $p_V = 0.48$ to assign diameters to objects lacking a measured size. If the canonical value of the beaming factor is used in fixed-η solutions of the family members, the resulting median geometric albedo is higher: $p_V = 0.58$. With this geometric albedo the result (confirmed and candidate family members excluding minimum and maximum velocities) is $\gamma = 0.46$, which indicates that the result is not sensitive to a moderate difference in the assumed geometric albedo.

The fitted values indicate that ejection velocities are dependent on diameter although in some of the cases the power-law slope is 0.5–0.6, which is higher than expected from theory. This means that smaller fragments of the Haumea family have been dispersed in the orbital element space much more than the currently known larger fragments (Lykawka et al. 2012). This may affect theories of the formation of the family that try to solve the problem of too low velocities: an average based on those velocities is probably biased by the fact that we have only observed, and discovered, the largest fragments of the family, which have lower velocities than smaller fragments.

4.4. Correlations

The small number of reliably measured Haumea family members and dynamical interlopers makes it challenging to detect correlations. The diameter and geometric albedo results (Table 5) suggest a positive correlation but, when taking into account the error bars (Peixinho et al. 2015), for the Haumea family objects we obtain a Spearman correlation coefficient of $\rho_{D\,p_V} = 0.65^{+0.22}_{-0.45}$ with a P-value of 0.40 (i.e. confidence level CL = 0.84 σ), being, therefore, not significant. For the eight dynamical interlopers (Table 8) the correlation strength appears weaker, but the evidence is of the same order as in the Haumea family members and also not significant: $\rho_{D\,p_V} = 0.37^{+0.38}_{-0.54}$ (P-value = 0.38; CL = 0.88 σ).

Nevertheless, some remarks about minimum sampling for detections can be made. Supposing that the correlation between effective diameters and geometric albedos among the Haumea family was $\rho = 0.9$, given our error bars and the low dispersion of albedos and diameters, such a correlation would be observationally "degraded" to ~0.65 (see Peixinho et al. 2015) and we would need a sample of $n \geq 39$ objects to have a risk lower than 10% of missing it, if we aim at a 3σ level detection. Analogously, regarding the dynamical interlopers, even if their true diameter-albedo correlation was $\rho = 0.4$, we would need a sample of $n \geq 112$ objects to ensure the detection. Most of the dynamical interlopers are classified as dynamically hot CKBOs and a sample of 26 objects in that class (excluding Haumea family and dwarf planets) showed no evidence of a diameter-albedo correlation at 3σ level taking into account the error bars (Vilenius et al. 2014).

To confirm that the diameter-albedo correlation among the Haumea family objects would indeed be different from the one among the dynamical interlopers, at a 3σ level, we would need to increase the sampling required to detect the presence of the correlations by a factor of 2.5 compared to the numbers of objects given above. The accuracy of size and albedo estimates can improve in the future, for example, by more stellar occultations. If the error bars were lower than ~5%, then a sample of 15 Haumea family objects and 112 dynamical interlopers would be enough to confirm a difference between $\rho = 0.9$ and $\rho = 0.4$ at a 3σ level.

5. Conclusions

We have measured the sizes and geometric albedos of three confirmed Haumea family members: 2003 OP_{32}, 2005 RR_{43}, and 2003 UZ_{117}. In addition, we have updated the results of 2002 TX_{300}, 1996 TO_{66}, 1995 SM_{55}, and 1999 KR_{16}. We have also refined or determined optical phase coefficients for several family members and candidate members and have determined the ejection velocities of 2008 AP_{129}, 2009 YE_7, and 2014 FT_{71}. The ejection velocity is inversely correlated with the fragment diameter, and therefore the Haumea family may be less compact than thought. An average ejection velocity is probably biased by the fact that we have only observed, and discovered, the largest fragments of the family, which have lower velocities than smaller fragments.

Our analysis has utilized the results of the stellar occultation by Haumea (Ortiz et al. 2017) and has the following main conclusions:

- Our measurements indicate that Haumea family members have a diversity of high to very high albedos and the lowest albedo among the detected objects is ~0.29 and the albedo limit of non-detected targets is $\gtrsim$0.2, which is higher than the average albedo of TNOs (~0.10). The median albedo of the Haumea family is $p_V = 0.48^{+0.28}_{-0.18}$. The highest-albedo member is 2002 TX_{300}.
- The median geometric albedo of probable dynamical interlopers in the Haumea family is $0.08^{+0.07}_{-0.05}$, consistent with that of the dynamically hot CKBO population, and much lower than that for the accepted family members. Object 2005 UQ_{513} does have an unusually high albedo (0.22), and two other objects (1999 CD_{158} and 2002 GH_{32}) have 2σ lower limits on their albedos of 0.13. Many Haumea family members and dynamical relatives lack albedo determinations, making interpretation of these albedo results tentative, but there is no strong evidence based on albedo that any of the dynamical interlopers should be considered as possible family members.
- Using measured sizes when available and an average albedo with optical absolute brightness for other family members, we determine the cumulative size distribution and find its slope to be $q = 3.2^{+0.7}_{-0.4}$ for diameters $175 < D < 300$ km. This is steeper than the slope of dynamically hot CKBOs in general in the same size range.
- We estimate the confirmed family members and the two moons to constitute 2.4% of the mass of Haumea.
- The ejection velocity depends on diameters of the fragments with a power-law slope of 0.21 (ignoring the minimum and maximum velocities). If candidate family members are included, to cover a broader diameter range, the slope is steeper: 0.50.
- We have determined Haumea's beaming factor: $\eta = 1.74^{+0.18}_{-0.17}$, which indicates a thermal inertia of $\Gamma \sim 1$ Jm^{-2} K^{-1} s$^{-\frac{1}{2}}$.

Acknowledgements. Part of this work was supported by the German *DLR* project number 50 OR 1108. T.M., C.K., P.S., and R.D. acknowledge that the research leading to these results has received funding from the European Union's Horizon 2020 Research and Innovation Programme, under Grant Agreement no 687378. A.P. acknowledges the grant LP2012-31 of the Hungarian Academy of Sciences. N.P. acknowledges funding by the Portuguese FCT - Foundation for Science and Technology (ref: SFRH/BGCT/113686/2015). CITEUC is funded by Portuguese National Funds through FCT – Foundation for Science and Technology (project: UID/ Multi/00611/2013) and FEDER – European Regional Development Fund through COMPETE 2020 – Operational Programme Competitiveness and Internationalisation (project: POCI-01-0145-FEDER-006922). C.K. has been supported by the K-125015 and GINOP-2.3.2-15-2016-00003 grants of the National Research, Development and Innovation Office (NKFIH, Hungary).

References

Altenhof, W. J., Bertoldi, F., & Menten, K. M. 2004, A&A, 415, 771
Alvarez-Candal, A., Pinilla-Alonso, N., Ortiz, J. L., et al. 2016, A&A, 586, A155
Balog, Z., Müller, T., Nielbock, M., et al. 2014, Exp. Astron., 37, 129
Barkume, K. M., Brown, M. E., & Schaller, E. L. 2006, ApJ, 640, L87
Barucci, M. A., Doressoundiram, A., Tholen, D., Fulchignoni, M., & Lazzarin, M. 1999, Icarus, 142, 476
Barucci, M. A., Alvarez-Candal, A., Merlin, F., et al. 2011, Icarus, 214, 297

Belskaya, I. N., Levasseur-Regourd, A.-C., Shkuratov, Y. G., & Muinonen, K. 2008, Surface Properties of Kuiper Belt Objects and Centaurs from Photometry and Polarimetry, eds. M. A. Barucci, H. Boehnhardt, D. P. Cruikshank, A. Morbidelli, & R. Dotson (Tucson, AZ: University of Arizona Press), 115
Benecchi, S. D., & Sheppard, S. S. 2013, AJ, 145, 124
Bessell, M. S., Castelli, F., & Plez, B. 1998, A&A, 333, 231
Boehnhardt, H., Tozzi, G. P., Birkle, K., et al. 2001, A&A, 378, 653
Boehnhardt, H., Delsanti, A., Barucci, A., et al. 2002, A&A, 395, 297
Boehnhardt, H., Schulz, D., Protopapa, S., & Götz, C. 2014, Earth Moon Planets, 114, 35
Braga-Ribas, F., Sicardy, B., Ortiz, J. L., et al. 2013, ApJ, 773, 26
Brown, M. E. 2012, Ann. Rev. Earth Planet. Sci., 40
Brown, M. E., Barkume, K. M., Ragozzine, D., & Schaller, E. L. 2007, Nature, 446, 294
Brown, M. E., Schaller, E. L., & Fraser, W. C. 2012, AJ, 143, 146
Brown, R. H. 1985, Icarus, 64, 53
Brown, R. H., Cruikshank, D. P., & Pendleton, Y. 1999, ApJ, 519, L101
Brucker, M. J., Grundy, W. M., Stansberry, J. A., et al. 2009, Icarus, 201, 284
Buratti, B. J., Hofgartner, J. D., Hicks, M. D., et al. 2017, Icarus, 287, 207
Campo Bagatin, A., Benavidez, P. G., Ortiz, J. L., & Gil-Hutton, R. 2016, MNRAS, 461, 2060
Carry, B., Snodgrass, C., Lacerda, P., Hainaut, O., & Dumas, C. 2012, A&A, 544, A137
Ćuk, M., Ragozzine, D., & Nesvorný, D. 2013, AJ, 146, 89
Davies, J. K., Green, S., McBride, N., et al. 2000, Icarus, 146, 253
Davis, D. R., & Farinella, P. 1997, Icarus, 125, 50
Delsanti, A. C., Boehnhardt, H., Barrera, L., et al. 2001, A&A, 380, 347
DeMeo, F. E., Fornasier, S., Barucci, M. A., et al. 2009, A&A, 493, 283
Dohnanyi, J. S. 1969, J. Geophys. Res., 74, 2531
Doressoundiram, A., Peixinho, N., de Bergh, C., et al. 2002, AJ, 124, 2279
Doressoundiram, A., Peixinho, N., Doucet, C., et al. 2005, Icarus, 174, 90
Doressoundiram, A., Boehnhardt, H., Tegler, S. C., & Trujillo, C. 2008, Color Properties and Trends of the Transneptunian Objects, eds. M. A. Barucci, H. Boehnhardt, D. P. Cruikshank, A. Morbidelli, & R. Dotson (Tuczon, AZ: University of Arizona Press), 91
Duffard, R., Ortiz, J. L., Thirouin, A., Santos-Sanz, P., & Morales, N. 2009, A&A, 505, 1283
Elliot, J. L., Kern, S. D., Clancy, K. B., et al. 2005, AJ, 129, 1117
Elliot, J. L., Person, M. J., Zuluaga, C. A., et al. 2010, Nature, 465, 897
Fornasier, S., Lellouch, E., Müller, T., et al. 2013, A&A, 555, A15
Fraser, W. C., & Brown, M. E. 2009, ApJ, 695, L1
Gil-Hutton, R., & Licandro, J. 2001, Icarus, 152, 246
Giorgini, J. D., Yeomans, D. K., Chamberlin, A. B., et al. 1996, BAAS, 28, 1158
Gladman, B., Kavelaars, J. J., Nicholson, P. D., Loredo, T. J., & Burns, J. A. 1998, AJ, 116, 2042
Gladman, B., Marsden, B. G., & Vanlaerhoven, C. 2008, Nomenclature in the Outer Solar System, eds. M. A. Barucci, H. Boehnhardt, D. P. Cruikshank, A. Morbidelli, & R. Dotson (Tucson, AZ: University of Arizona Press), 43
Griffin, M. J., Abergel, A., Abreu, A., et al. 2010, A&A, 518, L3
Grundy, W. M., Noll, K. S., & Stephens, D. C. 2005, Icarus, 176, 184
Hainaut, O. R., Delahodde, C. E., Boehnhardt, H., et al. 2000, A&A, 356, 1076
Hainaut, O. R., Boehnhardt, H., & Protopapa, S. 2012, A&A, 546, A115
Harris, A. W. 1998, Icarus, 131, 291
Hayes, D. S. 1985, in Calibration of Fundamental Stellar Quantities, eds. D. S. Hayes, L. E. Pasinetti, & A. G. D. Philip, IAU Symp., 111, 225
Hillier, J., Helfenstein, P., Verbiscer, A., et al. 1990, Science, 250, 419
Horner, J., Evans, N. W., & Bailey, M. E. 2004, MNRAS, 354, 798
Jewitt, D., & Luu, J. 1998, AJ, 115, 1667
Jewitt, D. C., & Luu, J. X. 2001, AJ, 122, 2099
Kiss, C., Müller, T. G., Vilenius, E., et al. 2014, Exp. Astron., 37, 161
Lacerda, P., Jewitt, D., & Peixinho, N. 2008, AJ, 135, 1749
Lacerda, P., Fornasier, S., Lellouch, E., et al. 2014a, ApJ, 793, L2
Lacerda, P., McNeill, A., & Peixinho, N. 2014b, MNRAS, 437, 3824
Leinhardt, Z. M., Marcus, R. A., & Stewart, S. T. 2010, ApJ, 714, 1789
Lellouch, E., Kiss, C., Santos-Sanz, P., et al. 2010, A&A, 518, L147
Lellouch, E., Santos-Sanz, P., Lacerda, P., et al. 2013, A&A, 557, A60
Lellouch, E., Moreno, R., Müller, T., et al. 2017, A&A, 608, A45
Levison, H. F., & Duncan, M. J. 1997, Icarus, 127, 13
Levison, H. F., Morbidelli, A., Van Laerhoven, C., Gomes, R., & Tsiganis, K. 2008a, Icarus, 196, 258
Levison, H. F., Morbidelli, A., Vokrouhlický, D., & Bottke, W. F. 2008b, AJ, 136, 1079
Licandro, J., di Fabrizio, L., Pinilla-Alonso, N., de León, J., & Oliva, E. 2006, A&A, 457, 329
Lockwood, A. C., Brown, M. E., & Stansberry, J. 2014, Earth Moon Planets, 111, 127
Lykawka, P. S., & Mukai, T. 2007, Icarus, 189, 213
Lykawka, P. S., Horner, J., Mukai, T., & Nakamura, A. M. 2012, MNRAS, 421, 1331
Marcus, R. A., Ragozzine, D., Murray-Clay, R. A., & Holman, M. J. 2011, ApJ, 733
Mommert, M. 2013, PhD Thesis, FU Berlin, Germany
Mommert, M., Harris, A. W., Kiss, C., et al. 2012, A&A, 541, A93
Mueller, M., Delbo', M., Hora, J. L., et al. 2011, AJ, 141, 109
Müller, T. G., Lellouch, E., Böhnhardt, H., et al. 2009, Earth Moon Planets, 105, 209
Ortiz, J. L., Sicardy, B., Braga-Ribas, F., et al. 2012a, Nature, 491, 566
Ortiz, J. L., Thirouin, A., Campo Bagatin, A., et al. 2012b, MNRAS, 419, 2315
Ortiz, J. L., Santos-Sanz, P., Sicardy, B., et al. 2017, Nature, 550, 219
Pál, A., Kiss, C., Müller, T. G., et al. 2012, A&A, 541, L6
Pál, A., Kiss, C., Müller, T. G., et al. 2016, AJ, 151, 117
Peixinho, N., Delsanti, A., & Doressoundiram, A. 2015, A&A, 577, A35
Perna, D., Barucci, M. A., Fornasier, S., et al. 2010, A&A, 510, A53
Perna, D., Dotto, E., Barucci, M. A., et al. 2013, A&A, 554, A49
Pilbratt, G. L., Riedinger, J. R., Passvogel, T., et al. 2010, A&A, 518, L1
Pinilla-Alonso, N., Brunetto, R., Licandro, J., et al. 2009, A&A, 496, 547
Poglitsch, A., Waelkens, C., Geis, N., et al. 2010, A&A, 518, L2
Rabinowitz, D. L., Barkume, K., Brown, M. E., et al. 2006, ApJ, 639, 1238
Rabinowitz, D. L., Schaefer, B. E., & Tourtellotte, S. W. 2007, AJ, 133, 26
Rabinowitz, D. L., Schaefer, B. E., Schaefer, M., & Tourtellotte, S. W. 2008, AJ, 136, 1502
Ragozzine, D., & Brown, M. E. 2007, AJ, 134, 2160
Ragozzine, D., & Brown, M. E. 2009, AJ, 137, 4766
Rieke, G. H., Young, E. T., Engelbracht, C. W., et al. 2004, ApJS, 154, 25
Romanishin, W., & Tegler, S. C. 1999, Nature, 398
Santos-Sanz, P., Lellouch, E., Fornasier, S., et al. 2012, A&A, 541, A92
Santos-Sanz, P., Lellouch, E., Groussin, O., et al. 2017, A&A, 604, A95
Schaefer, B. E., Rabinowitz, D. L., & Tourtellotte, S. W. 2009, AJ, 137, 129
Schaller, E. L., & Brown, M. E. 2008, ApJ, 684, L107
Schlichting, H. E., & Sari, R. 2009, ApJ, 700, 1242
Sheppard, S. S. 2010, AJ, 139, 1394
Sheppard, S. S., & Jewitt, D. C. 2002, AJ, 124, 1757
Sheppard, S. S., & Jewitt, D. C. 2003, Earth Moon Planets, 92, 207
Sicardy, B., Ortiz, J. L., Assafin, M., et al. 2011, Nature, 478, 493
Snodgrass, C., Carry, B., Dumas, C., & Hainaut, O. 2010, A&A, 511, A72
Spencer, J. R., Lebofsky, L. A., & Sykes, M. V. 1989, Icarus, 78, 337
Stansberry, J. A., Gordon, K. D., Bhattacharya, B., et al. 2007, PASP, 119, 1038
Stansberry, J., Grundy, W., Brown, M., et al. 2008, Physical Properties of Kuiper Belt and Centaur Objects: Constraints from the *Spitzer* Space Telescope, eds. M. A. Barucci, H. Boehnhardt, D. P. Cruikshank, A. Morbidelli, & R. Dotson (Tucson, AZ: University of Arizona Press), 161
Tegler, S. C., & Romanishin, W. 2000, Nature, 407, 979
Thirouin, A., Ortiz, J. L., Duffard, R., et al. 2010, A&A, 522, A93
Thirouin, A., Ortiz, J. L., Campo Bagatin, A., et al. 2012, MNRAS, 424, 3156
Thirouin, A., Sheppard, S. S., Noll, K., et al. 2016, AJ, 151, 148
Trujillo, C. A., & Brown, M. E. 2002, ApJ, 566, L125
Trujillo, C. A., Sheppard, S. S., & Schaller, E. L. 2011, ApJ, 730, 105
Vilenius, E., Kiss, C., Mommert, M., et al. 2012, A&A, 541, A94
Vilenius, E., Kiss, C., Müller, T., et al. 2014, A&A, 564, A35
Volk, K., & Malhotra, R. 2011, ApJ, 736, 11
Volk, K., & Malhotra, R. 2012, Icarus, 221, 106
Werner, M. W., Roellig, T. L., Low, F. J., et al. 2004, ApJS, 154, 1
Zappala, V., Cellino, A., Dell Oro, A., & Paolicchi, P. 2002, Physical and Dynamical Properties of Asteroid Families, eds. W. F. Bottke, A. Cellino, A. Paolicchi, & R. P. Binzel (Tucson, AZ: University of Arizona Press), 619